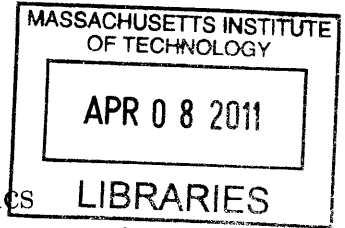# Flow-induced oscillation of flexible bodies

by

Peter Buchak

Submitted to the Department of Mathematics
in partial fulfillment of the requirements for the degree of

Doctor of Philosophy

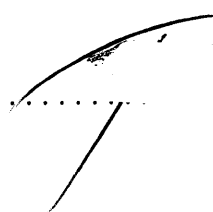at the

MASSACHUSETTS INSTITUTE OF TECHNOLOGY

September 2010

© Peter Buchak, MMX. All rights reserved.

Author . . . .
Department of Mathematics
August 20, 2010

Certified by . . . .
John W. M. Bush
Professor
Thesis Supervisor

Accepted by . . . .
Michel X. Goemans
Chairman, Applied Mathematics Committee

Accepted by . . . .
Bjorn Poonen
Chairman, Department Committee on Graduate Students

Flow-induced oscillation of flexible bodies

by

Peter Buchak

Submitted to the Department of Mathematics
on August 20, 2010, in partial fulfillment of the
requirements for the degree of
Doctor of Philosophy

Abstract

We present a combined theoretical and experimental investigation of two systems in which flexible bodies are induced to oscillate by steady flows. The first system we study consists of multiple thin sheets of paper in a steady flow, clamped at the downstream end, which we call the "clapping book". Pages sequentially lift off, accumulating in a stack of paper held up by the wind. When the elasticity and weight of the pages overcome the aerodynamic force, the book claps shut; this process then repeats. We investigate this system experimentally and theoretically, using the theory of beams in high Reynolds number flow, and test our predictions of the clapping period.

The second system we consider is inspired by free-reed musical instruments, which produce sound by the oscillation of reeds, thin strips of metal tuned to specific pitches. Each reed is mounted above a slot on the upstream side of a support plate, a geometry that allows a steady flow to induce finite-amplitude oscillations. We study this system experimentally and propose models, also based on the theory of elastic beams in high Reynolds number flow. The relative merits of these models is assessed by comparing their predictions with experiments.

Thesis Supervisor: John W. M. Bush
Title: Professor

Acknowledgments

The author would like to acknowledge Tristan Gilet, Alex Hornstein, and Shaunalynn Duffy for help with, and discussions about, the experiments. For help with videos, the author acknowledges Denis Terwagne and the MIT Edgerton Center's Jim Bales.

Contents

Chapter 1

Introduction

Flow past flexible structures arises in many settings in nature and industry. The applicability of fluid dynamics to biology has been responsible for much recent interest in the motion of flexible bodies in ambient flow [50][12]. One example is animal locomotion, where thrust is often generated by bending. Examples of high Reynolds number flight include that of birds and insects [51] and the passive flight of seedpods [48]. Swimming has also been studied extensively, both at high and low Reynolds numbers. Classic works on high Reynolds number swimming include those of Taylor [49] and Lighthill [35]. Flexibility is also important at low Reynolds number, a classic introduction to which is given by Purcell [42]. Many microorganisms use cilia and flagella to move [40], one exotic example being Volvox [24].

Fluid-structure interaction is also relevant to plants. The effect of wind forcing on plant canopies has been studied [43][23] with the goal of elucidating the factors influencing wind damage to crops, a problem with enormous consequences in agriculture. Similarly, the flow through marshes has been modeled [27]. This class of problems is not limited to flexible structures suspended in fluid. The fluid mechanics of blood in the circulatory system [50][39] has consequences in medicine; this in turn has motivated an interest in flow through flexible tubes [32][41][8][11].

The ubiquity of such examples in nature, as well as in industrial applications, has prompted the study of several canonical problems involving flexible bodies in flow. The flapping flag is perhaps the most comprehensively studied [5][2][6][37]. More

6

complex geometries, including arrays of multiple flag-like objects, have also been considered [45]. The problem of tree leaves curling up in high wind, which reduces the drag on the tree and its risk of being uprooted, has been studied in the context of the bending of a flexible fiber in a soap film [3][4].

In the current work, we study two systems, both consisting of flexible solid structures induced to oscillate by fluid flow. First, we introduce what we refer to as the "clapping book", a system that can be observed by setting a book outside on a table on a windy day. Our book consists of a stack of multiple pages clamped at one end and placed in a wind tunnel. As illustrated in Fig. 2-1, the wind causes the pages to lift off from the book and form a bent stack of paper, which eventually claps shut. This process occurs repeatedly with a well-defined period of several seconds. We seek to understand the essential dynamics: what governs the shape of the stack of pages, how quickly pages accumulate, what causes them to collapse, and how long it takes before returning to its initial position. Work has been done on similar systems, including Lighthill's work on slender fish[35] and recent work on flexible filaments [46], but little analogous work has been done on systems containing multiple such structures. In chapter 2, we describe the clapping book, including the experiments, the theoretical model, and our comparisons between experiments and theory. This work has been submitted to Phys. Rev. Lett.[10]

Then we turn our attention to free reeds, which are responsible for producing sound in "free reed aerophone" musical instruments. This family of instruments, which includes the accordion, concertina, harmonica, harmonium, and reed organ, was primarily developed in the early 1800's by a number of inventors; the concertina is noteworthy in that it was invented by the scientist Sir Charles Wheatstone. The origin of free reeds can be traced to the far East, but a Western free reed is essentially a flexible metal beam clamped at one end to a support plate, out of which is cut a slot into which the reed can bend; see Figs. 3-1 through 3-3 for photos and a diagram. A steady flow of air, provided for example by a set of bellows or a player's lungs, causes the reed to vibrate, producing the desired pitch.

Rayleigh, in "The Theory of Sound"[44], includes a chapter (8) on the lateral

(transverse) vibration of beams, which can be applied to air-driven reeds, but also to other instruments such as the Jew's harp and the xylophone. Rayleigh also introduced (Section 68a) a nonlinear ODE frequently quoted in textbooks as a model of the clarinet reed, although it is not considered physically realistic. Reed-driven wind instruments were first discussed by Helmholtz [29], who introduced a classification system that included "inward-striking" reeds, such as the clarinet reed, oboe reed, and free reeds, and also "outward-striking" reeds, which referred to brass instruments, in which the lips play the role of the reed. The acoustics of woodwind instruments with reeds has been studied by Backus [7], in the context of the clarinet, and by Fletcher [25]. Fletcher and Rossing devote a chapter in their text [26] to reeds, including a section on free reeds.

Cottingham and coworkers have done extensive experimental work on the acoustics of free reeds, both those of Western free reed instruments (which we treat exclusively) and Asian free reed instruments, many of which also have pipes coupled to the reed. They made measurements of the oscillation, including the waveform, spectrum, and shape of air-driven organ reeds [16] and accordion reeds [15], and an analysis of their modes of vibration. They also measured the dependence of a reed's frequency on the driving pressure [17]. All these results directly inform our work. One of these authors' additional areas of focus is the physics of free reeds coupled to pipes. In this context they address the phenomenon of pitch bending [14], a technique by which harmonica players can change the note played by a free reed. Pitch bending is also addressed elsewhere [31].

The only work addressing the fluid dynamics of free reeds appears to be that of St. Hilaire, Wilson, and Beavers [30]. These authors perform flow visualization experiments and measurements of vibration amplitude growth, and present a flow model from which they obtain qualitative agreement with their measurements. In the current work, we wish to improve upon their model by retaining more of the realistic features of free reeds. In chapter 3, we introduce free reeds, reviewing previous work and describing our experiments. In chapter 4, we use recent developments in the theory of conformal maps on multiply connected domains [21] to solve for the flow

field under the assumption of ideal flow [19]. Finally, in chapter 5, we develop an improved theory and compare its predictions with our measurements. The results of chapters 3 and 5 are to be submitted for publication [9].

The clapping book and free reed share several common features. In both problems, the challenge is to understand why oscillations occur and how to predict measurable quantities such as their frequency. To correctly explain their behavior, we will need to consider finite-amplitude deformations of the flexible structure, as well as the role of fluid viscosity. Both systems involve structures that can be described using the theory of elastic beams and flows characterized by a high Reynolds number. As a consequence, similar models will be developed to describe the systems.

Chapter 2

The clapping book

Here, we introduce a novel model system, the *clapping book*, which we can describe predictively. The *book*, a horizontal stack of sheets of paper clamped at one end, is placed in a wind tunnel with the clamped end downstream. Representative photographs of the book's behavior under wind loading are presented in Fig. 2-1a-e. The pages lift off (Fig. 2-1a-d) and form a bent stack of paper held up by the wind. As pages accumulate, this elevated stack thickens and moves progressively further upstream. Eventually the book *claps* shut and this process restarts (Fig 2-1e) resulting in continuous oscillations with a well-defined period. We develop a theoretical model to explain this behavior quantitatively and perform a series of detailed comparisons with our experiments.

2.1 Model for page deformation

Each elevated page is modeled as a single inextensible elastic beam whose motion is confined to the xy plane (Fig. 2-1f). The beam has length L, width $W \ll L$, and thickness $h \ll W$. Its mass per unit length is $\rho_p h W$ and its bending stiffness is $B = Eh^3/12(1 - \nu^2)$, where ρ_p is the beam's density, E its Young's modulus, and ν its Poisson ratio. The beam's shape is represented by $\mathbf{x}(s,t)$, with unit tangent $\mathbf{x}_s = \mathbf{t} = (\cos \theta, \sin \theta)$ and normal $\mathbf{n}$, by convention pointing counterclockwise with respect to the tangent. Its evolution is governed by the relation between curvature
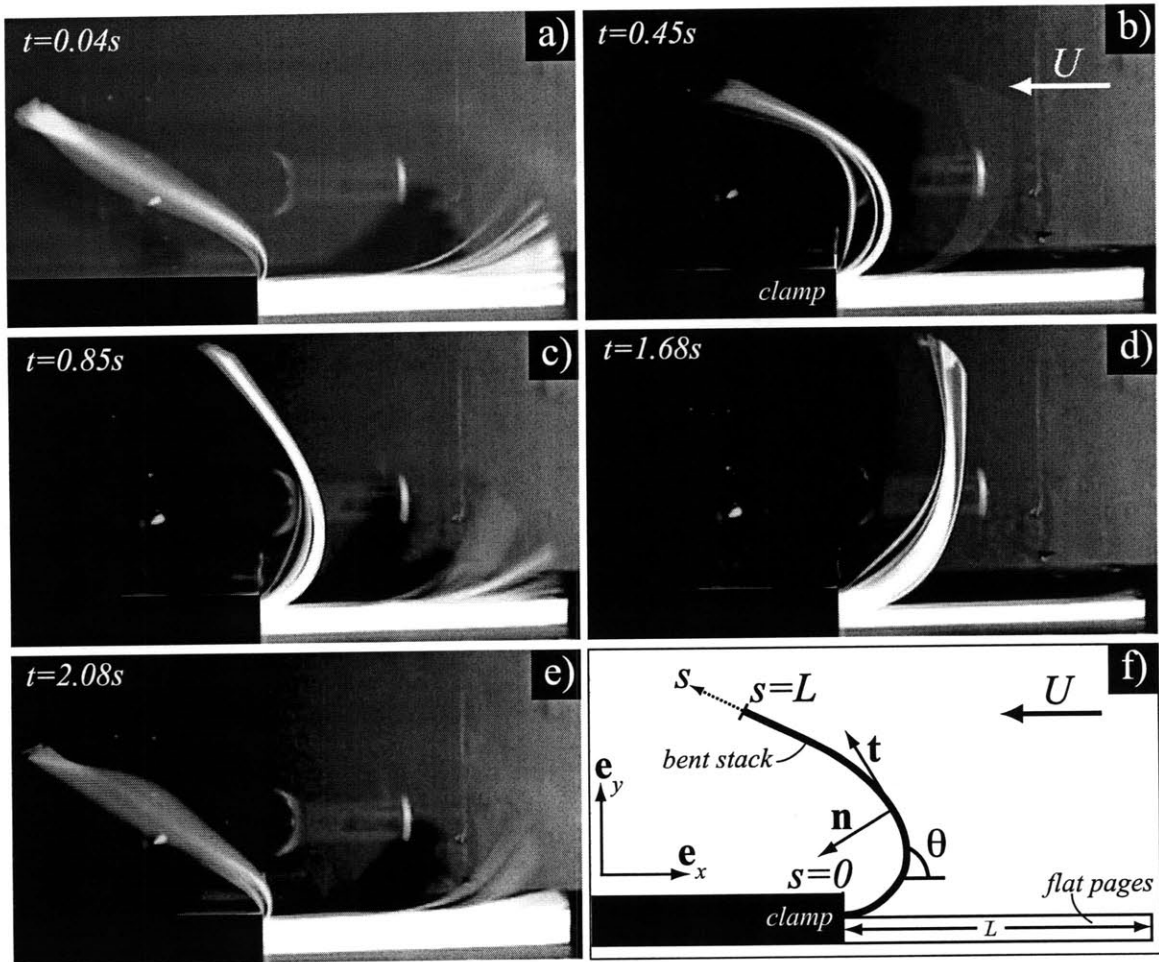
Figure 2-1: (a-e) Representative photographs of the clapping book at selected times during a single period. (f) Schematic diagram of the system.

and torque and the angular and linear momentum equations, which can respectively be written in dimensionless form as

$$\theta_s = \Gamma, \tag{2.1}$$

$$I\theta_{tt} = \Gamma_s + \mathbf{n} \cdot \mathbf{F}, \tag{2.2}$$

$$\mathbf{x}_{tt} = \mathbf{F}_s + K\mathbf{n} - \Delta\mathbf{e}_y, \tag{2.3}$$

where the arclength s and position $\mathbf{x}$ are scaled by L, and time t by $\sqrt{\rho_p h L^4/B}$. The z-component of the internal torque (Γ), the internal force ($\mathbf{F}$), and the aerodynamic force per unit length (K) are scaled by BW/L, BW/L^2 and BW/L^3, respectively. Equivalent equations have been given by Landau and Lifshitz [34] and by Coleman, Dill, Lembo, Lu, and Tobias [13], although not in this form.

This non-dimensionalization results in two dimensionless parameters,

$$I = \frac{h^2}{12L^2} \tag{2.4}$$

$$\Delta = \frac{\rho_p g h L^3}{B}. \tag{2.5}$$

Δ, the elastogravity number, represents the weight of the pages relative to their bending rigidity. The pages are thin relative to their length, $I \ll 1$, and the corresponding term in Eq (2.2) is therefore dropped for the remainder of this work. This yields a model equivalent to the flag described by Alben and Shelley [5].

At the clamped end of the beam, the position is fixed and its tangent is horizontal:

$$\mathbf{x}\big|_{s=0} = \mathbf{0} \tag{2.6}$$

$$\theta\big|_{s=0} = 0. \tag{2.7}$$

At the free end, the internal torque and force must vanish:

$$\Gamma\big|_{s=1} = 0 \tag{2.8}$$

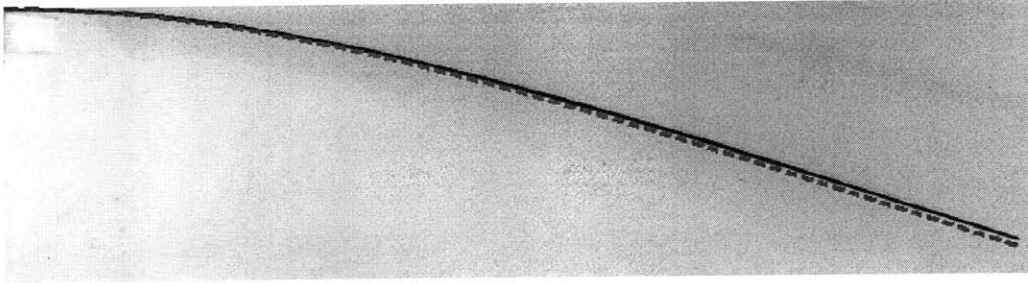$$\mathbf{F}\big|_{s=1} = \mathbf{0}. \tag{2.9}$$

Figure 2-2: Photograph of a single acetate sheet (solid line) with $L = 17.1$ cm, $W = 2.9$ cm, $\rho_p h W = 0.114$ g/cm, and $BW = 2.8 \times 10^{-4}$ Nm^2, hanging off the edge of a table in the absence of flow, superimposed with the predicted shape. For all static shape calculations, we use a spatial resolution of 1000.

Before considering the aerodynamic force K, we test our model for the pages in the absence of flow. In Fig. 2-2, we present a photograph of a single sheet hanging off the edge of a table and superimpose the equilibrium shape predicted by the model, showing excellent agreement.

2.2   Flow model

To describe the flow around the pages, we focus on the case in which $W \ll L$. This allows us to use the slender body theory used by Schouveiler, Eloy, and Le Gal [46]. We take the wind in the far field to have uniform velocity $-U\mathbf{e}_x$. Viscous drag can be neglected since the Reynolds number based on page length ranges from 4×10^4 to 2×10^5. In the wind's frame of reference, the beam's shape is given by $\mathbf{X}(s,t) = \mathbf{x}(s,t) + Ut\mathbf{e}_x$ and the flow is determined entirely by the normal component of the beam's velocity,

$$V = \mathbf{n} \cdot \mathbf{X}_t = \mathbf{n} \cdot \mathbf{x}_t + U\mathbf{n} \cdot \mathbf{e}_x. \tag{2.10}$$

In the regime of interest, the speed of the pages is much slower than that of the flow: The wind speeds U at which the dynamic experiments were run were at least 6 m/s; in contrast, we estimate that it took at least half a second for the beam to turn an angle of $\pi/2$, which would make for a velocity $\mathbf{x}_t$ at a radius of 0.2 m of at most 0.6 m/s. Therefore, for simplicity, we neglect the time derivative term in

13

Eq. (2.10); this is accurate except where the beam is nearly horizontal, in which case the accuracy of the flow model is questionable anyway due to the presence of the table.

We consider two components of the external aerodynamic force on the beam, the *resistive* and the *reactive* forces. The *resistive force* on an element of the beam is the drag experienced by a flat plate moving in the direction of its normal, with magnitude per unit length

$$F_1 = \frac{1}{2} C_d \rho_a V^2 W \tag{2.11}$$

$$= \frac{1}{2} C_d \rho_a W (\mathbf{n} \cdot \mathbf{x}_t - U \sin \theta)^2, \tag{2.12}$$

where ρ_a is the density of air and C_d is a drag coefficient that must be determined experimentally. Assuming the flow reaches a steady state faster than the beam moves, any other contribution from the unsteadiness of the flow can be neglected. As mentioned above, for our simulations, we neglect the first term in Eq. (2.12).

The *reactive force* arises as the fluid accelerates to follow the shape of the beam. Following Lighthill [35], we take the flow locally to be the potential flow induced by a flat plate moving in the direction of its normal. This flow has momentum $\mathbf{P} = \rho_a A V \mathbf{n}$, where $\rho_a A$ is the beam's added mass, with $A = \pi (W/2)^2$ being the area of its circumscribing circle. The change in the fluid momentum at a fixed point in the moving frame is the sum of its change in time and its change as one looks in the $-U\mathbf{e}_x$ direction, $\mathbf{P}_t - (U\mathbf{e}_x \cdot \nabla)\mathbf{P}$. Since the flow changes in the tangential direction by $\mathbf{P}_s$ and does not change in the normal direction, the second term can be evaluated $(U\mathbf{e}_x \cdot \mathbf{t})\mathbf{P}_s$. The $-\mathbf{n}$ component of the change in the fluid momentum gives the magnitude of the reactive force (per unit length) on the beam,

$$F_2 = -\rho_a A (V_t - (U\cos\theta)V_s) \tag{2.13}$$

$$= \frac{\pi}{4} \rho_a W^2 \left((\mathbf{t} \cdot \mathbf{x}_t + U\cos\theta)(\theta_t - U\cos\theta\,\theta_s) - \mathbf{n} \cdot \mathbf{x}_{tt} + U\cos\theta\,\theta_t \right). \tag{2.14}$$

Again, the relatively low speed of the pages allows the time derivative term in

Eq. (2.13) to be neglected: Assume that, for wind speeds U of at least 6 m/s, the value of V varies fairly uniformly between 0 and U over the distance 0.2 m and over a time at least 0.5 s, so that its time and spatial derivatives can be approximated by dividing by these time and length scales. Then the ratio V_t/UV_s of the magnitudes of the time and spatial derivatives in Eq. (2.13) is at most 0.07, so the first term is negligible compared to the second as long as the page isn't nearly vertical so that $cos\ \theta$ isn't too small. When the page is nearly vertical, the ratio AV_t/WU^2 of the magnitude of the time derivative term in Eq. (2.13) to the magnitude of Eq. (2.12) is at most 0.01. In either case, it should be safe to neglect the time derivative of V in Eq. (2.13). Thus, we keep only the $U^2\ cos^2\theta\ \theta_s$ term in Eq. (2.14).

The total aerodynamic force on the beam is the sum of the resistive and reactive forces, $F_1 + F_2$. This can be expressed in dimensionless form as

$$K = \frac{1}{2} C_d C_y sin^2\theta - \frac{\pi}{4} \lambda C_y cos^2\theta \frac{d\theta}{ds}, \qquad (2.15)$$

where terms have been dropped for our system as described above. Two more dimensionless parameters have been introduced:

$$C_y = \frac{\rho_a U^2 L^3}{B} \qquad (2.16)$$

$$\lambda = \frac{W}{L}. \qquad (2.17)$$

C_y is the Cauchy number, the dimensionless ratio of aerodynamic force $\rho_a U^2 WL$ to bending force BW/L^2, and λ is the aspect ratio of the beam.

Our model has four parameters, Δ, λ, C_y, and C_d. The drag coefficient, C_d, is the only parameter that must be determined by fitting to experiments (described below). The approximate ranges of the other parameters in our experiments are $0.1 < \Delta < 20$, $0.1 < \lambda < 0.5$, and $C_y < 60$. Given values for these parameters, the static shape of a beam at equilibrium in the wind can be computed by solving Eqs. (2.1-2.3,2.15) with the time derivative terms dropped. In Fig. 2-3, we present photographs of the experimental shapes of a single elastic sheet at three wind speeds and superimpose

15

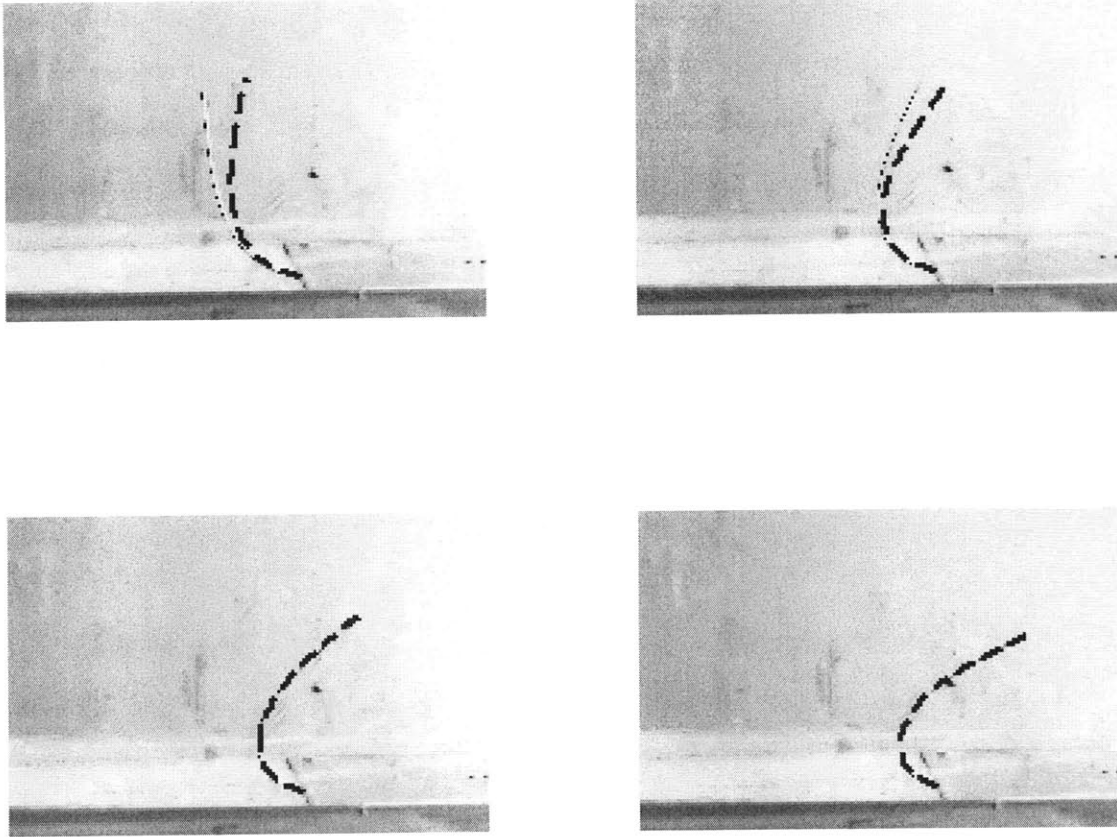Figure 2-3: Photographs of a single acetate sheet (solid lines), with $L = 15.0\,cm$, $W = 2.9\,cm$, $\rho_p hW = 0.114\,g/cm$, and $BW = 2.4 \times 10^{-4}\,Nm^2$, superimposed with predicted shapes (dashed lines). Flow speeds were 5.3, 6.8, 8.4, and 11.1 m/s.

the shapes predicted by our model, showing satisfactory agreement.

2.3   Critical wind speed

In the experiments, as U is decreased, we observe that there is a critical wind speed below which a given sheet can no longer be supported. In Fig. 2-4, we show measurements of the critical wind speed for a strip of acetate and a strip of vinylpolysiloxane (VPS), as L is varied.[1] This phenomenon is captured in our model; for given values of Δ, λ, and C_d, Eqs. (2.1-2.3,2.15) fail to have a valid equilibrium solution when C_y is below a critical value C_y^*. Hence, from Eq. (2.16), a critical wind speed $U = U^*$ is predicted. We compare the experimentally measured critical wind speeds with those predicted by our model (Fig. 2-4), where the drag coefficient C_d is treated as the single fitting parameter. In subsequent calculations, we use the average value that best fits each material, $C_d = 1.76 \pm 0.03$, which is consistent with previously reported experimental measurements of the drag coefficient for a flat plate [36].

2.4   Page accumulation

Having presented a model for a single wind-loaded sheet, we return to the clapping book to understand its periodic behavior. At any one time, we consider some of the book's pages to be lifted up, forming a stack bent by the wind, while the rest remain flat. When the elevated stack contains more pages than the wind can support, the book claps shut. We proceed by separately considering three aspects of the process: (i) page accumulation, (ii) loss of support of the bent pages, and (iii) the subsequent collapse.

A schematic diagram of the expected flow profile over the flat stack is sketched in Fig. 2-5, with recirculation zones shown ahead of the step and on the surface of the

---

[1]Our wind tunnel was not sensitive enough to provide consistent wind at low enough speeds to measure the critical speed for a single piece of paper, necessitating the use of other materials. The use of a VPS strip is a more complete test of the model than the acetate strip because the parameter Δ is basically constant for the acetate strip, while it varies for the different lengths of the VPS; thus the predicted critical Cauchy number C_y^* is not a constant for the VPS.
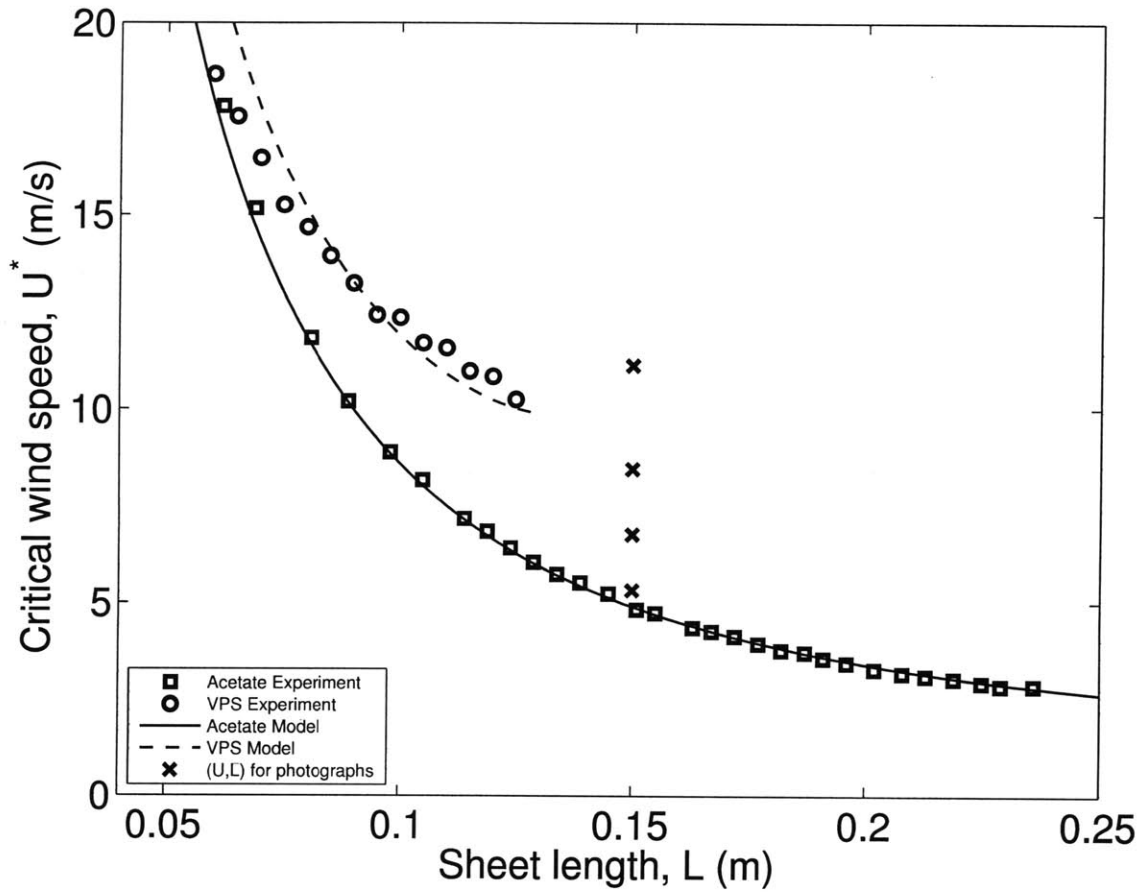
17

Figure 2-4: Measured and predicted critical wind speeds for varying-length strips of two materials. Lower: acetate strip with $W = 3.0\,cm$, $\rho_p hW = 0.118\,g/cm$, and $BW = 2.6 \times 10^{-4}\,Nm^2$. Upper: VPS strip with $W = 2.2\,cm$, $\rho_p hW = 2.04\,g/cm$, and $BW = 2.3 \times 10^{-4}\,Nm^2$, with paper on its front surface. Error in wind speed measurements is around 1%. The value of the drag coefficient used here, $C_d = 1.76 \pm 0.03$, is the average of the value that best fit the acetate and the value that best fit the VPS. Also shown ($\times$) are the parameter values for the photographs in Fig. 2-3.
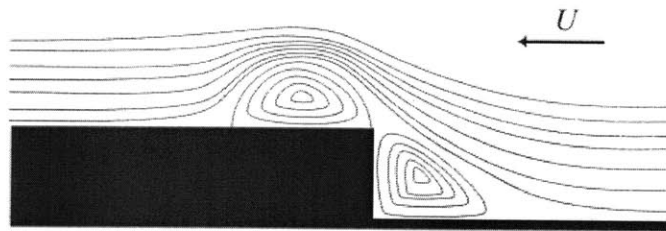

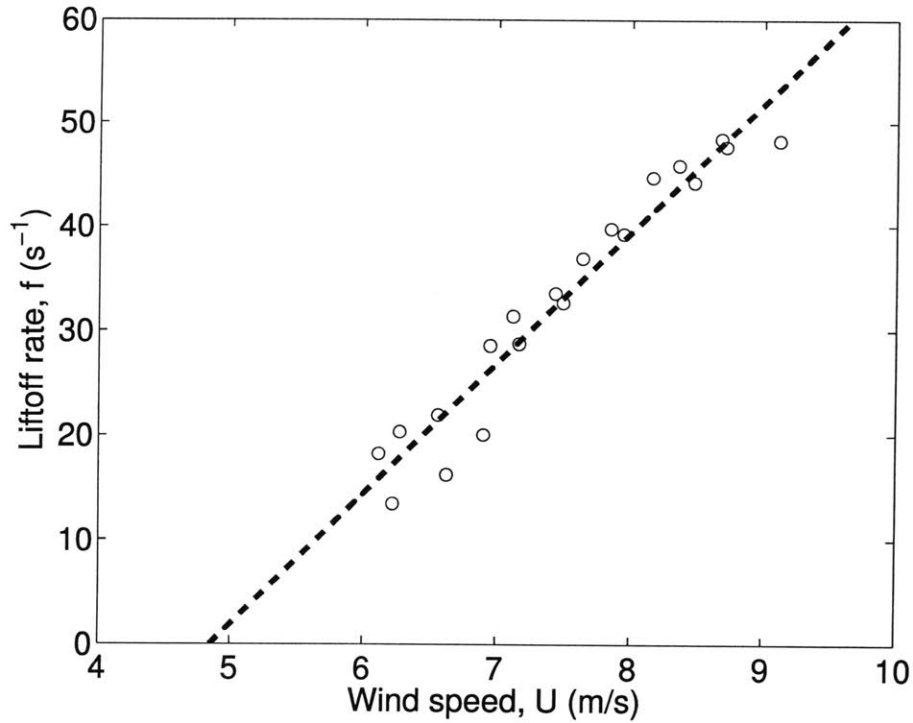Figure 2-5: Illustration of recirculation zones in the flow over the flat stack of pages.

Figure 2-6: Measured page liftoff rate averaged over 10 oscillations, for a paper book of 150 pages of dimensions $L = 17.0\,cm$ and $W = 2.8\,cm$, with $\rho_p hW = 0.021\,g/cm$ and $BW = 8.2 \times 10^{-6}\,Nm^2$. Error in liftoff rate measurements is about 2%. The dashed line is the liftoff rate given by Eq. (2.18) with constants $\beta = 12.5\,m^{-1}$ and $U_0 = 4.9\,m/s$.

top page. This geometry is known as the forward-facing step and has been studied both experimentally [47] and computationally [52]. A detailed analysis of the flow would involve determining the precise locations of flow separation and reattachment, a challenging endeavor that goes beyond the scope of our study.

Instead, we proceed by deducing an empirical relation for the page liftoff rate. We focus on the regime in which the wind speed is high enough that the pages lift off continuously. In this regime, we expect the rate at which new pages lift off to be set by the rate at which previous pages are convected a sufficient distance by the wind, which should scale with the wind speed U, after accounting for a minimum wind speed U_0. In Fig. 2-6, we present experimental measurements of the dependence of the liftoff rate, f, on wind speed for a particular book. We find that f is well described
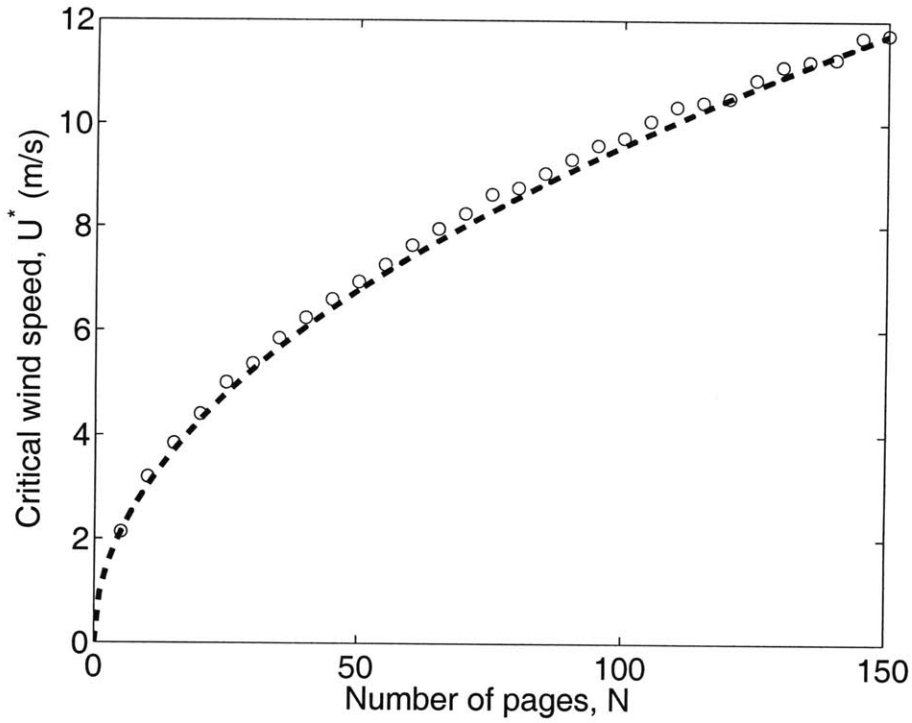
Figure 2-7: Critical wind speed measured for an elevated stack of N pages, for the book described in Fig. 2-6. The model gives $C_y^* = 18.5$, from which the critical wind speed is calculated (solid line) using Eq. (2.19), as $U^* = \sqrt{NBC_y^*/\rho_a L^3}$.

by the linear relationship,

$$f = \beta(U - U_0), \tag{2.18}$$

with $\beta = 12.5 \pm 0.8\ m^{-1}$ and $U_0 = 4.9 \pm 0.2\ m/s$ (Fig. 2-6).

2.5 Loss of support

We proceed by determining the maximum number of pages that the wind can support, using the equilibrium model for a beam introduced above, Eqs. (2.1-2.3,2.15), after dropping the time derivatives. The elevated pages are treated as a single beam, and we assume that the pages slide against each other without friction. As such, the bending energy of the stack of elevated pages is simply the sum of the bending energies of the individual pages. Thus, if $\rho_p hW$ and B characterize a single page, the elastic beam representing the entire elevated stack of N pages has mass per unit length $N\rho_p hW$

20

and bending stiffness NB.[2] We note that, from Eqs. (2.5,2.17), both parameters Δ and λ are then independent of N. Hence, since the model's prediction for C_y^* depends only on Δ and λ, this prediction should be unique for a particular book, regardless of how many pages have been lifted up. Using this C_y^*, Eq. (2.16) yields a relation between the number of pages in a stack, N, and the critical wind speed, U^*:

$$C_y^* = \frac{\rho_a U^{*2} L^3}{NB}. \tag{2.19}$$

In Fig. 2-7, we show that this prediction is in excellent agreement with the experimentally measured critical wind speeds and provides a validation of our description of the behavior of multiple pages. Conversely, for a given wind speed U, we use Eq. (2.19) to obtain the number of pages, N^*, for which U is the critical speed. This is the maximum number of pages this wind speed can support.

2.6   Page collapse

Once this maximum number of pages is exceeded, stability is lost and the bent stack collapses. We simulate the collapsing stack of pages as a beam using the full time-dependent form of Eqs. (2.1-2.3,2.15).

We choose initial conditions that take into account the momentum of the pages as collapse begins. Recall that there is an equilibrium shape for a given number of pages, which changes as pages accumulate. Near collapse, we observe the actual shape of the pages to oscillate around the equilibrium shape with a period comparable to the natural period P of the first mode of an unforced elastic beam. In our nondimensionalization, $P = 2\pi/m^2$, with the constant $m = 1.88$ given by Rayleigh [44]. We simulate the case when the maximum number of pages N^* is reached when the beam is exactly at its peak position in the oscillation, a quarter of a period before it would pass through the critical position. The initial shape for the simulation can then be taken to be the equilibrium shape at a time $P/4$ before the maximum number of pages

---

[2]If the pages were to stick together without sliding, the beam's thickness would scale with N, resulting in a bending stiffness that scales with N^3.
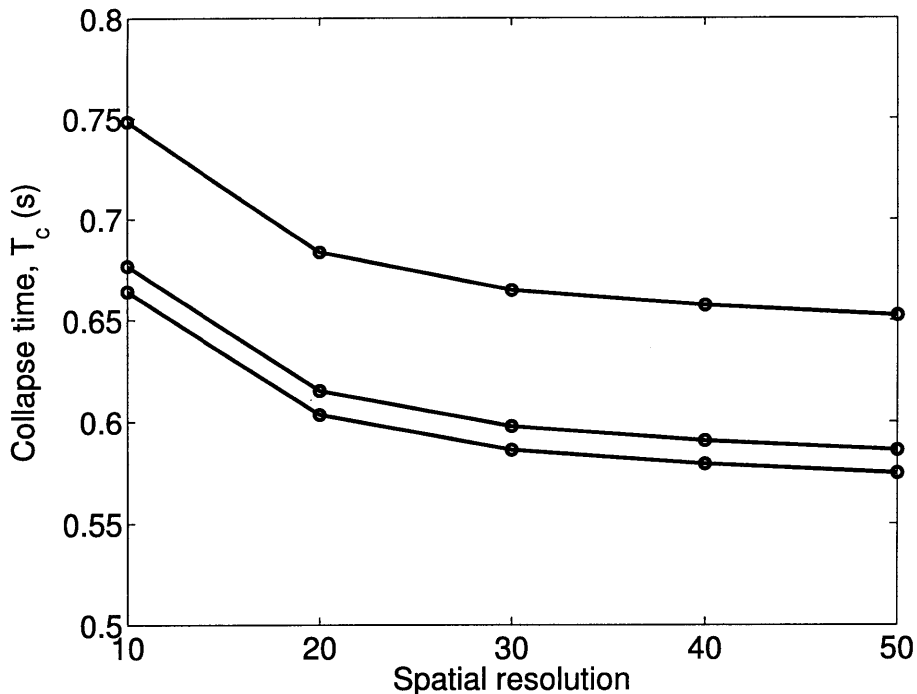
21

Figure 2-8: Convergence of collapse time T_c for minimum, middle, and maximum wind speeds used in the experiments (upper, middle, and lower lines, respectively) as spatial resolution is varied. The collapse time is longer for lower wind speeds because the pages have less initial momentum. (Recall that the Cauchy number used for the simulation is C_y^*, the same for all wind speeds.) For each spatial resolution, all the results were recalculated, including fitting the drag coefficient. For 50 points of spatial resolution, we used a dimensionless time step of 5×10^{-8}.

has accumulated, with no initial velocity. This would be the equilibrium shape with Cauchy number calculated with bending stiffness $N_{IC}B$, where $N_{IC} = N^* - fP/4$.

In reality, the maximum number of pages could be reached at any point during the oscillation, not necessarily when the beam is at its peak position. Therefore, the simulated collapse time would have to be adjusted depending on where in the oscillation the critical number of pages is reached. The possible range of this adjustment will be taken to be the uncertainty in the collapse time, described shortly.

We denote by T_c the time at which the tip of the page becomes horizontal in the simulations. This occurs nearly simultaneously with the rest of the page becoming horizontal, as expected from observations. For simplicity, we used the collapse simulation run at the middle wind speed used in the experiments, finding that the collapse

22

time T_c for the minimum and maximum wind speeds differs by less than 0.1 s. In Fig. 2-8, we plot the convergence of the middle, minimum, and maximum wind speeds as the spatial resolution is varied, and choose the value for the middle wind speed at the highest of these resolutions, $T_c = 0.59$ s. This agrees roughly with the collapse time estimated from frame-by-frame analysis of one of the videos, 0.61 s.

2.6.1 Collapse simulation

To simulate collapse, we solve Eqs. (2.1-2.3,2.15) numerically, with the following method: Consider the beam to be made up of straight segments and vertices. Starting from the clamped end, number the segments and vertices, with the first movable segment and the first movable vertex (directly after the first segment) each numbered 1. The last segment and last vertex, which is at the very end of the beam, are numbered N. Each segment n is described by a tangent angle θ_n, from which the unit tangent and unit normal vectors can be calculated, and has associated with it an internal force $\mathbf{F}_n$. Each vertex n is described by a position $\mathbf{x}_n$, and we assume that the aerodynamic force K_n can be calculated at each vertex given the instantaneous shape of the beam, to be described later.

At each time step, all values of θ and θ_t are known from the current shape of the beam. From these, all values of K along the beam can be calculated. These known quantities are used to construct a system of equations to be solved for the unknowns $\mathbf{F}$, $\mathbf{x}_{tt}$, and θ_{tt} along the beam, a total of $5N$ unknown quantities. This system consists of three equations to be described below, the torque balance equation, the momentum equation, and the geometric relation between θ and $\mathbf{x}$. Because these last two equations have two components each, this is a total of $5N$ equations. Once the equations are solved, the values of θ_{tt} are integrated to obtain θ_t at the next time step.

The torque balance equation can be obtained by substituting the s derivative of Eq. (2.1) into Eq.(2.2), which gives $\theta_{ss} + \mathbf{n} \cdot \mathbf{F} = 0$. The discrete version of this

23

equation, evaluated on segment n, is

$$\frac{\theta_{n+1} - 2\theta_n + \theta_{n-1}}{ds^2} + \mathbf{n}_n \cdot \mathbf{F}_n = 0,$$

for n ranging from 1 through N. The discrete versions of boundary conditions (2.7,2.8),

$$\begin{aligned} \theta_0 &= 0 \\ \theta_{N+1} &= \theta_N, \end{aligned}$$

are needed to evaluate θ_0 and θ_{N+1}.

The discrete version of Eq. (2.3), evaluated on vertex n, is

$$\mathbf{x}_{tt\ n} = \frac{\mathbf{F}_{n+1} - \mathbf{F}_n}{ds} + K_n \mathbf{n}_n - \Delta \mathbf{e}_y,$$

for n ranging from 1 through N. The discrete version of boundary condition (2.9),

$$\mathbf{F}_{N+1} = \mathbf{0},$$

is needed for $\mathbf{F}_{N+1}$.

A third equation is required to relate the values of θ and $\mathbf{x}$. Taking two time derivatives of the geometric relation defining the unit tangent vector, $\mathbf{x}_s = \mathbf{t}$, gives the equation

$$\mathbf{x}_{tts} = -\theta_t^2 \mathbf{t} + \theta_{tt} \mathbf{n}.$$

The discrete version of this relation, evaluated on segment n, is

$$\frac{\mathbf{x}_{tt\ n} - \mathbf{x}_{tt\ n-1}}{ds} = -\theta_{t\ n}^2 \mathbf{t}_n + \theta_{tt\ n} \mathbf{n}_n,$$

for n ranging from 1 through N. The discrete version of boundary condition (2.6),

$$\mathbf{x}_0 = \mathbf{0},$$

24

is needed to take $\mathbf{x}_{tt\ 0} = \mathbf{0}$.

2.6.2   Uncertainty in collapse time

Represent the "position" of the page around the equilibrium by

$$A \sin \frac{2\pi}{P}t,$$

so different times in the oscillation can be referred to by t values varying from 0 to P. Assume the oscillation amplitude is small enough that the "potential well" in which the page oscillates transitions instantaneously to a "slope" at the instant the maximum number of pages is reached; that is, the page doesn't oscillate so far upstream that it starts collapsing before the critical instant. This should be true if the pages accumulate fast enough.

Suppose that the critical instant is reached at a time t in the oscillation. We must add to (subtract from) the simulated collapse time whatever amount of time is necessary to get the actual collapse time. First, we must account for the fact that the simulation is started from a stationary position, while in reality the page may be moving at the critical instant. If the page is moving up at the critical instant, we must add the time required for the page to decelerate. If it's moving down, we must subtract the time it has already accelerated. The amount of time to add is

$$T_1(t) = \left\{ \begin{array}{ll} P/4 - t, & 0 \le t \le P/2 \\ t - 3P/4, & P/2 \le t \le P \end{array} \right\},$$

which ranges between $-P/4$ and $P/4$.

If we've added time, we now have to calculate the collapse time for a stationary page in the position it decelerated to. If instead we've subtracted time, we have to calculate the collapse time for a stationary page in the position the page would have

accelerated from. This stationary position is:

$$x(t) = \begin{cases} A, & 0 \le t \le P/2 \\ A - \frac{8A}{P}(t - P/2), & P/2 \le t \le 3P/4 \\ -A + \frac{8A}{P}(t - 3P/4), & 3P/4 \le t \le P \end{cases}$$

Since the collapse simulation is started at the maximum amplitude A, we have to subtract the amount of time it takes the page to fall a distance $A - x(t)$. We take the page to fall at a constant speed equal to the maximum speed in the oscillation, $v = 2\pi A/P$. The time to fall this distance would then be

$$-T_2(t) = \frac{A - x(t)}{v} = \frac{A}{v} \begin{cases} 0, & 0 \le t \le P/2 \\ \frac{8}{P}(t - P/2), & P/2 \le t \le 3P/4 \\ 2 - \frac{8}{P}(t - 3P/4), & 3P/4 \le t \le P \end{cases},$$

which ranges from 0 to a maximum of $2A/v$ at $t = 3P/4$.

The total time to add to the simulated collapse time is $T_1(t) + T_2(t)$, which has a maximum value of $P/4$ and a minimum value of $min(-P/4, -2A/v) = -P/\pi$ (using the value of v above). This gives the range of uncertainty of the collapse time,

$$[T_c - P/\pi, T_c + P/4]. \tag{2.20}$$

2.7 Clapping period

Having described the accumulation and collapse of the pages, these results can be combined to calculate the total clapping period, which is a representative and readily quantifiable feature of the clapping process. The duration of accumulation can be taken to be the maximum number of pages that can be supported, N^* calculated by Eq. (2.19), divided by the rate at which pages accumulate, f from Eq. (2.18). This is added to the duration of collapse, T_c, to give the complete clapping period,

$$T = \frac{N^*}{f} + T_c. \tag{2.21}$$

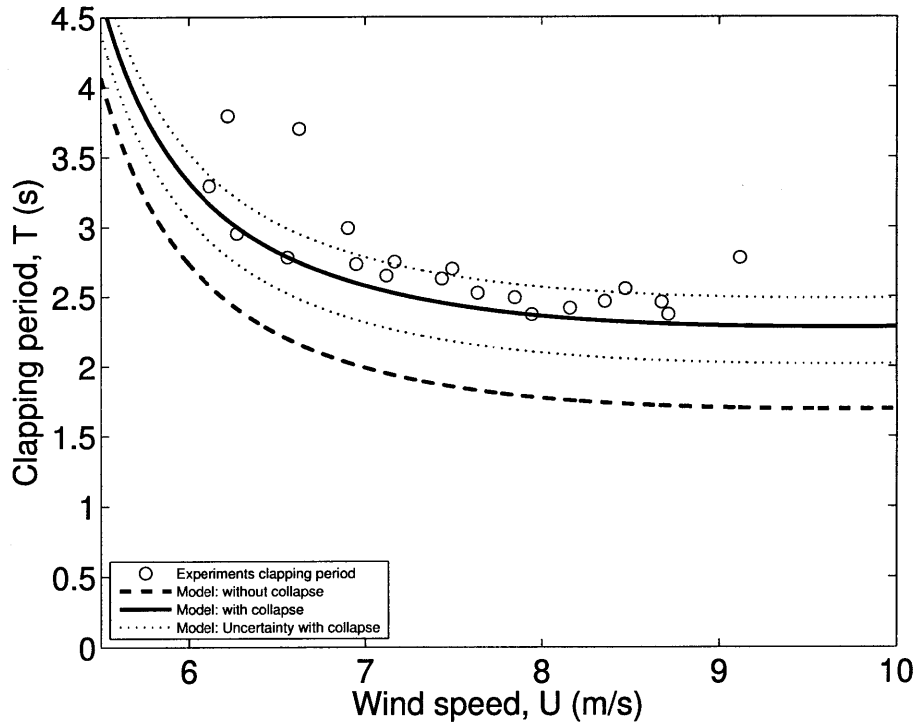Figure 2-9: Measured clapping period as a function of wind speed for the book described in Fig. 2-6, averaged over 10 oscillations, compared with the prediction from Eq. (2.21). The dashed line is the first term of Eq. (2.21); the solid line incorporates the collapse time as well. The dotted lines indicate the range of uncertainty in the prediction, Eq. (2.20). Error in clapping period measurements is about 2%.
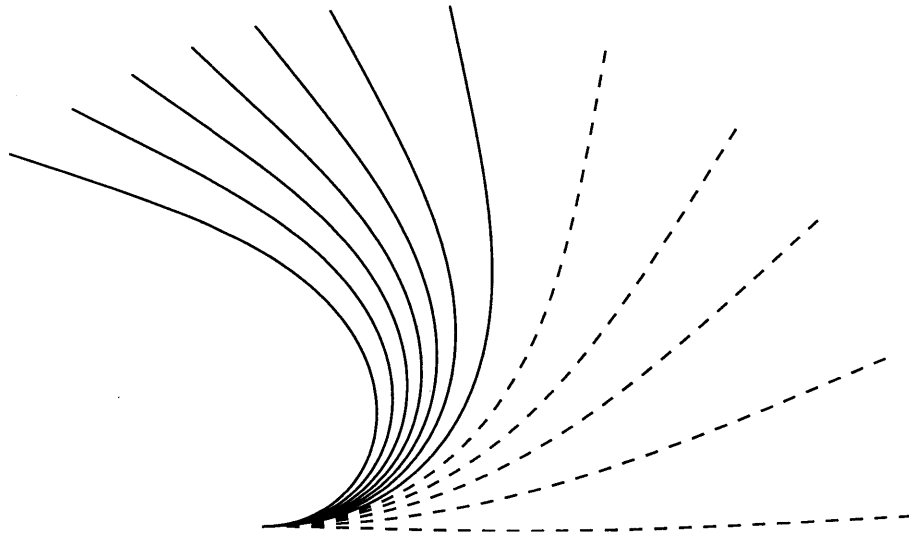
Figure 2-10: Simulated snapshots of the bent stack of pages during the clapping process for $U = 6$ m/s, at selected times after pages begin to accumulate. The solid and dashed lines are equilibrium shapes during page accumulation and snapshots during collapse, respectively. The times for the snapshots are 0.9, 1.2, 1.5, 1.8, 2.1, 2.4, and 2.7 s (accumulation) and 3.11, 3.21, 3.25, 3.29, and 3.32 s (collapse).

In Fig. 2-9 we show the measured clapping period for a book as a function of U, which is in good agreement with our theoretical prediction. In Fig. 2-10 we present representative calculated page shapes over the course of an oscillation, which compare well with the photographs in Fig. 2-1.

2.8 Conclusion

We have introduced a novel system that exhibits a robust oscillatory behavior. Excellent agreement is obtained between experiment and theory. This instance of fluid-structure interaction was a priori far from trivial since the flow profile couples in a nonlinear way to the large elastic deformations of the multiple pages. Nonetheless, the problem was made tractable by reduction to a set of fundamental ingredients required for a predictive description. We hope that our model system will provide insight into other problems involving multiple flexible structures and flow, which are abundant in the natural world.

Chapter 3

Free reeds: background and experiment

3.1 Introduction

Western free reeds are flexible beams, usually made of steel or brass, riveted to a support plate. The plate has a slot cut out of it into which the reed can bend. A leather valve usually covers the other side of the slot to prevent air flow through the reed when not being played. Many support plates have two reeds, one on each side of the plate. If both slots have valves, each side of the support plate will have one reed and one valve. Figs. 3-1-3-2 show a free reed from an accordion on its support

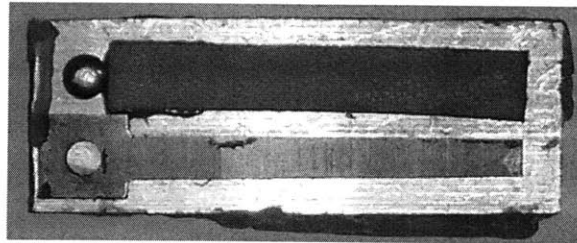Figure 3-1: Photograph of an accordion reed on its support plate. The reed itself is the metal strip on the lower half of the plate, riveted to the plate in the lower lefthand corner. When the reed vibrates, it moves in an out of a slot cut into its support plate (not visible in this photograph). On the upper half of the support plate is a leather valve covering a slot for a similar reed on the opposite side of the plate.
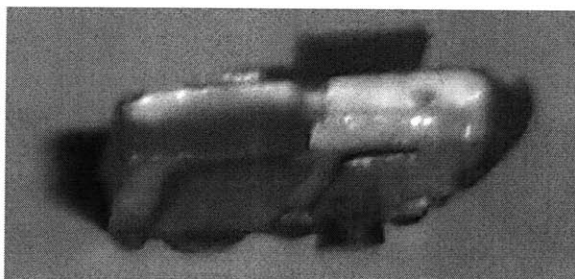
Figure 3-2: The reed and support plate from Fig. 3-1, looking from the end on. In this photo, the reeds on both sides of the support plate are visible, as well as the leather valve opposite each reed. Air flow in the downward direction would cause the reed on the top of the plate to oscillate, while the reed on the bottom remains silent. Similarly, flow in the upward direction would cause only the bottom reed to oscillate.

Figure 3-3: Schematic cross section of the left half of the support plate from Fig. 3-2, with the reed on the top of the plate. In this diagram, the slot through which the reed vibrates is visible. The valve for this reed, which would normally be on the bottom of the support plate, is omitted from this drawing. Air flow in the downward direction would make this reed oscillate, while air flow in the upward direction would not.

plate; the valve for the other reed is also visible. Fig. 3-3 illustrates a reed and the slot into which it bends.

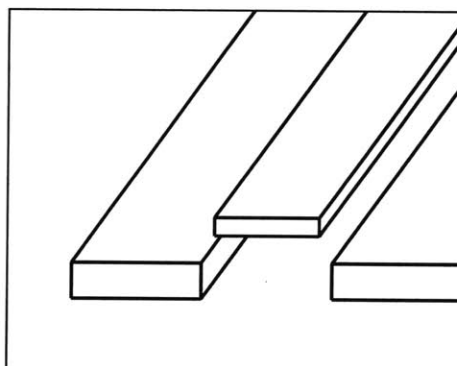Free reeds are designed to oscillate when driven by a flow. Fig. 3-4 shows snapshots of a free reed during oscillation. At its peak (first frame), the reed tip's distance from the support plate is several times its thickness. At its lowest position (third frame), the tip of the reed is below the upper surface of the support plate.

It is a well known peculiarity of Western free reeds that they only work in one direction; that is, a reed will only oscillate if attached to the upstream side of the support plate. If the flow direction is reversed, the reed remains silent. This is why each support plate used for accordion, concertina, and harmonica reeds supports two reeds, one on each side; one reed is designed to oscillate in one flow direction ("pushing" or "blowing"), the other reed in the other direction ("pulling" or "drawing"). Note that the leather valves pictured in Fig. 3-1 and Fig. 3-2 do prevent air from flowing in the reverse direction, but this is simply to prevent needless air loss; when a valve is absent, as is the case for some reeds, the reed still only works with the proper airflow direction.

The fact that only upstream reeds work has important implications for musical instrument design. The note layout of the earliest accordions and harmonicas is arranged so that each button or hole plays two adjacent notes of the scale, one for each direction of air flow. For such instruments, the fact that reversing the air flow changes the note is an advantage, letting the player play more notes with less movement. Other accordions and concertinas play the same note regardless of the direction of the air flow. For such instruments, each hole must have two reeds tuned to the same pitch. These instruments have (at least) twice the number of reeds as notes, resulting in larger weight and cost. Furthermore, the two reeds for a note often go out of tune with each other, causing a noticeable change in pitch when the air flow is reversed.

In addition to the condition that a reed be on the upstream side of its support plate, a further requirement for a reed to oscillate is that it lie close to its support plate. Typically, the space between the tip of the reed and the plate is comparable
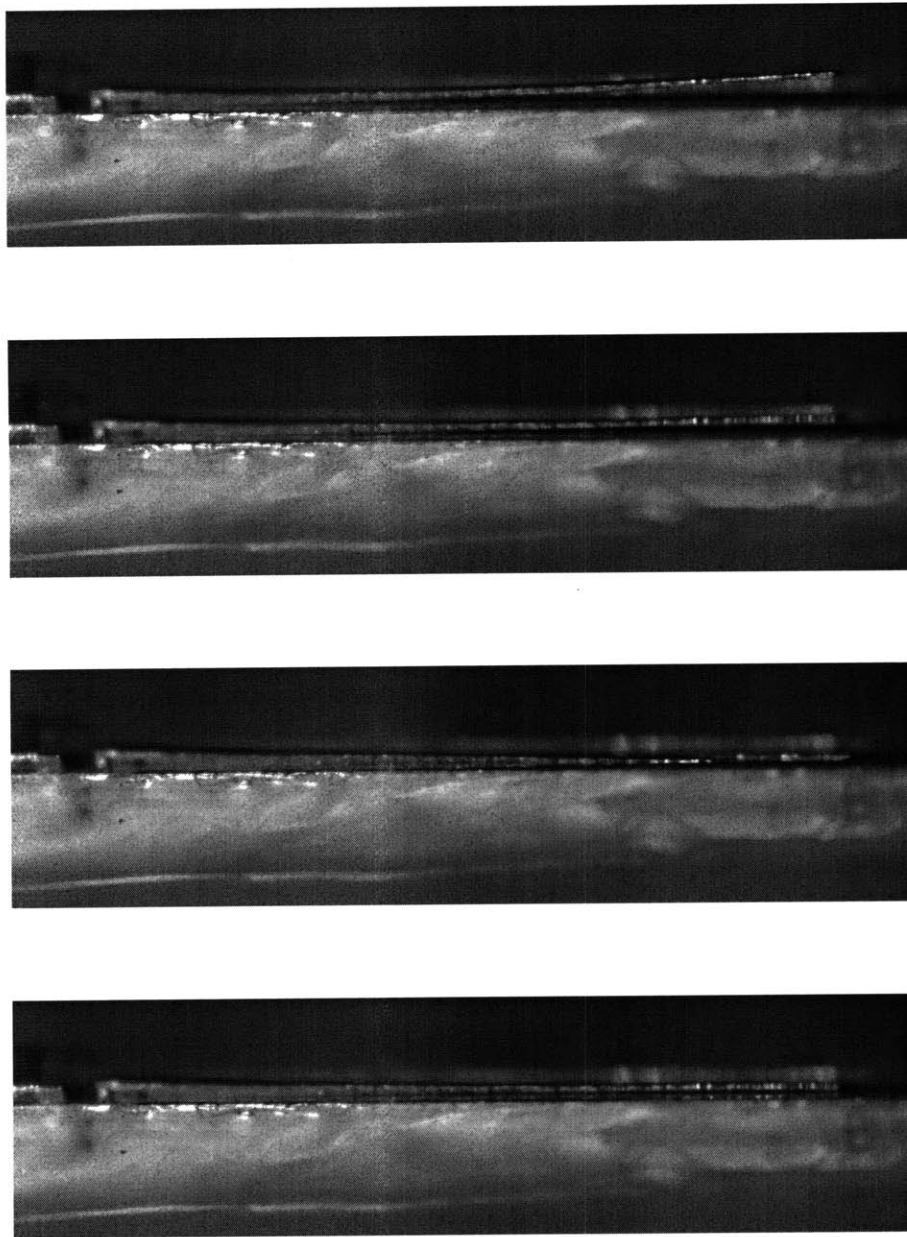
Figure 3-4: Snapshots from a video of an oscillating accordion reed, viewed from the side. In the first frame, the tip of the reed is approximately at its peak position above the support plate. In the second, it is moving downward towards the support plate. In the third frame, the tip of the reed has passed below the top of the support plate and is no longer visible in the photo. In the final frame, the reed is moving back towards its initial position. These photos were taken 0.0003 s apart, with air flowing from top to bottom. The amplitude of oscillation can be estimated from this video to be several times the reed's thickness, on the order of one or two millimeters.

to the thickness of the reed itself.

The fact that the behavior of the reed depends on its position relative to the support plate suggests that this support plate serves a larger role than just anchoring the reed. It is clear that in order to explain the oscillation of a free reed, the geometry of the reed and support plate together must be studied. We seek to elucidate the mechanism by which a steady flow induces oscillations in this geometry.

3.2   Previous work

St. Hilaire, Wilson, and Beavers [30] were the first to study the fluid dynamics of air-driven free reed instruments, which they did in the context of the harmonium (reed organ). They performed flow visualization studies in water, which were an important first step toward understanding the nature of the flow around free reeds. They observed the flow to separate from the reed at its edges, forming a wake downstream of the reed. This is the expected behavior for flow past a flat plate at high Reynolds number [38]. An important conclusion the authors drew from their experimental work is that an instability in the flow itself is unlikely to be responsible for driving the reed's oscillation. Although they observed vortices behind the reed, the frequency of vortex shedding was not consistent with the frequency of the reed itself. In addition, they observed that, at the early stages of oscillation, the amplitude of oscillation grows exponentially, indicating a driving force linear in the reed's current amplitude. This suggests a mechanism that depends on the reed's changing configuration, rather than the flow.

St. Hilaire et al. also presented a model for the flow. They classified the flow into several regions, each described in terms of potential flow, with the pressure matched at the boundary between each region. Their model gave approximately correct predictions for the force on the reed. One major drawback of their model is that it is based on the assumption of small-amplitude oscillations. Their characterizations of the flow in each region, and the boundaries on which the matching was performed, were also somewhat arbitrary. Moreover, their analysis incorporated many ingredi-

Parameter	Symbol	Value	How obtained
length	L	2.27 cm	measured directly
width	W	0.2 cm	estimate near reed tip
thickness	h	0.05 cm	calculated from natural frequency
unforced tip height	a_0	0.02 cm	measured directly
clearance area	B	0.01 cm^2	estimate
density	ρ_r	8 g/cm^3	standard value for steel
Young's modulus	E	2×10^{12} $gcm^{-1}s^{-2}$	standard value for steel
natural frequency	f	750.1 Hz	Fourier transform of sound recording

Table 3.1: Geometry of the accordion reed used in our experiments. Accordion reeds do not generally have uniform width and thickness, so those values should be regarded as averages.

ents, making it difficult to isolate the mechanism responsible for oscillations. In this work, we adopt a different approach in order to avoid these difficulties. For example, we will treat the reed as a flexible beam, rather than simply a flat plate, making it easier to compare with experiment.

Our work is also informed by other experimental work. Cottingham, Lilly, and Reed [16] showed that the shape of an organ reed during oscillation is described well by the shape of the first mode of an unforced beam, whose formula is given by Rayleigh [44]. We will use this observation to simplify our analysis. Cottingham [15] also measured the position of an accordion reed as a function of time, finding it to be nearly sinusoidal. We will use this as a check for our theory.

3.3 Measurements

We performed measurements on an F#5 free reed obtained from a piano accordion; values of the relevant parameters are listed in Table 3.1. The reed was waxed into an appropriately-sized hole in a chamber and driven by compressed air. The main chamber we used has rough dimensions 10 cm × 10 cm × 30 cm, for a volume of approximately $V_c \approx 3000$ cm^3, although we made measurements with other chambers as well. Our chamber was fed by a 1 $cm = 2r_h$ diameter hose, approximately $L_h \approx 4\,m$ long, attached to a source of compressed air.

We explored the reed's behavior during oscillation using a microphone and a

sound recording, plucked reed

sound recording, 1.7 kPa

pressure measurement, 0.4 kPa

pressure measurement, 1.0 kPa
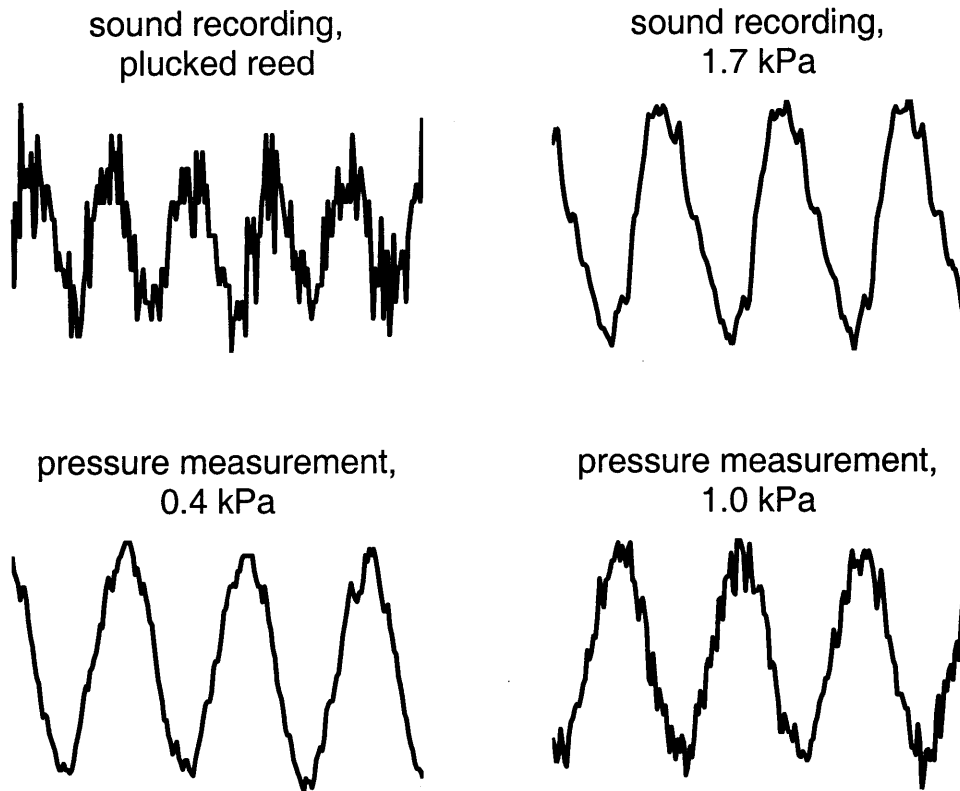
Figure 3-5: Waveforms associated with an oscillating free reed. The two upper plots are from sounds recordings made with a microphone of the reed being plucked outside the chamber (left) and the reed waxed into the chamber and driven with compressed air at a pressure of 1.7 kPa (right). The microphone was positioned inside the chamber in the second plot. The lower plots are data taken with a pressure sensor positioned inside the chamber, for two driving pressures. The frequency of all waveforms is close to the reed's natural frequency, 750 Hz. We did not measure the amplitude of oscillation, but observed the reed's maximum displacement from its initial position to be on the order of a millimeter or two.

pressure sensor. We used a recording of the reed being plucked to determine its natural frequency f, which we in turn used to obtain its thickness h from the values of its other parameters. We also made a recording of its sound when driven in our setup, and took data from a pressure sensor. Representative waveforms from these recordings are shown in Fig. 3-5.

Cottingham, Reed, and Busha made measurements of the dependence of frequency on driving pressure for a reed from a reed organ [17]. They found that at normal playing pressures, the frequency decreases approximately linearly with increasing pressure. In order to make similar measurements for our reed, we extracted the frequency from sound recordings at varying pressure, which we show in Fig. 3-6, lowest line. We were able to fit our measurements well with a line of negative slope, consistent with the previous authors' work. We did find that this line intersects the $p = 0$ axis below the reed's natural frequency, possibly because some amount of damping is present even with very low flow.

In order to detect any dependence on the geometry of the chamber, we also made frequency versus pressure measurements with our reed in different chambers. These measurements are shown in Fig. 3-6 as well. The slope is fairly consistent across experiments, $-2.0 \pm 0.4\ Hz/kPa$. The variation that does exist in the slope seems not to be correlated with the size of the chamber; in fact, three experiments using the same chamber showed a large variation. We conclude from this that the systematic error from one experiment to the next exceeds any variation due to the size of the chamber. This may be related to the variation in the way the reed was waxed into the chamber, which was done again for each new experiment.

3.4 Direction of study

Our goal is to elucidate the mechanism by which a steady flow induces oscillations in free reeds. As noted, the work of St. Hilaire, Wilson, and Beavers indicates that the force responsible for driving the reed depends on the reed configuration as it changes in time rather than on any instability of the flow. This suggests that a quasistatic model
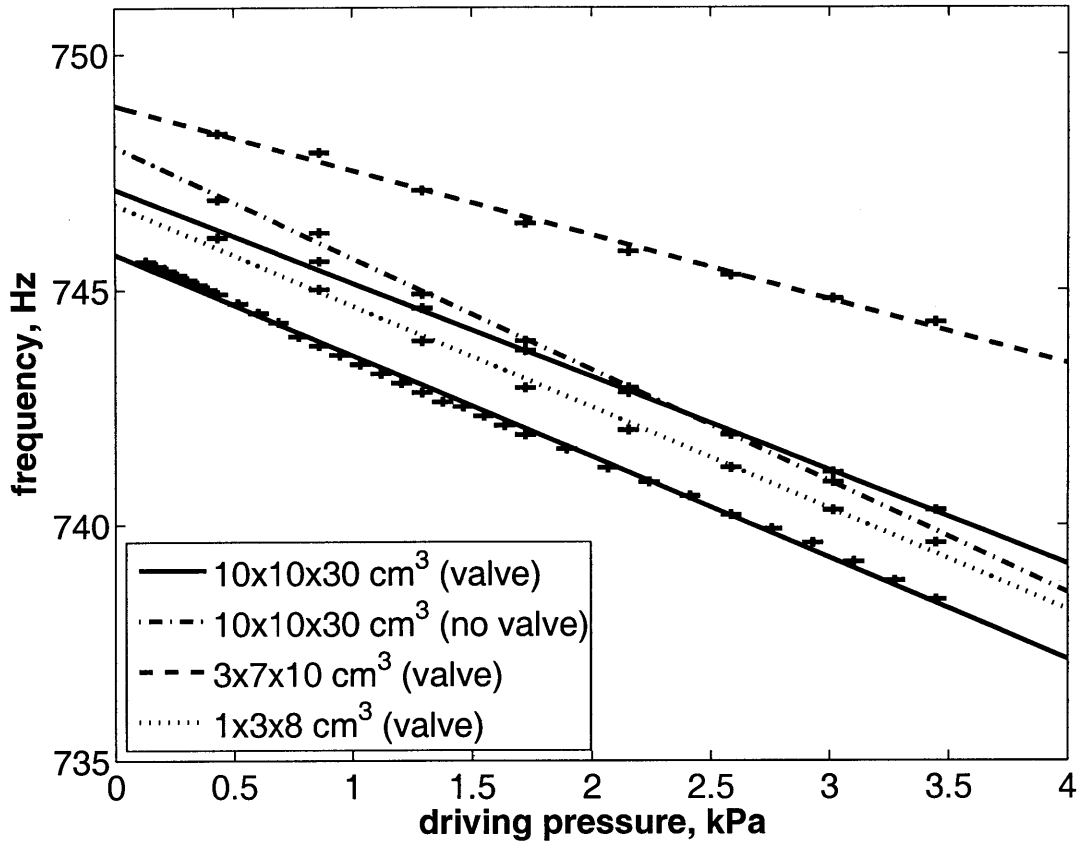
Chamber area	Chamber length	Slope	
$10x10\ cm^2$	$30\ cm$	$-2.15\ Hz/kPa$	(lower line, obtained first)
$10x10\ cm^2$	$30\ cm$	$-1.99\ Hz/kPa$	(higher line, obtained later)
$10x10\ cm^2$	$30\ cm$	$-2.37\ Hz/kPa$	(after leather valve removed)
$3x7\ cm^2$	$10\ cm$	$-1.37\ Hz/kPa$	
$1x3\ cm^2$	$8\ cm$	$-2.15\ Hz/kPa$	

Figure 3-6: The dependence of frequency on driving pressure of the accordion reed described in Table 3.1, waxed into chambers of various cross sectional areas and lengths. The best fit line is also shown, with its slope indicated. For the first four experiments, the leather valve covering the silent reed (shown in Figs. 3-1 and 3-2) was left on. For the final experiment, it was removed from the support plate and the slot covered with wax to prevent air loss. Frequencies were obtained from FFT's of 10 s long sound recordings. Measurement error is indicated by marker size.

37

for the flow may be sufficient to understand the reed's dynamics. We start by looking for a model in which the flow, and therefore the force, is determined completely by the reed's current position and velocity. In order to amplify oscillations, our model must contain some unsteadiness. Two possibilities for this source of unsteadiness will be described in Chapters 4 and 5.

We proceed in Chapter 4 by solving for the flow field under the assumption that the rate of air flow through the reed gap is constant. We further assume that the flow is two-dimensional, irrotational, and incompressible, which allows us to employ a conformal mapping technique. Our results direct us towards a source of unsteadiness that may be responsible for inducing oscillations, specifically, the force due to the acceleration of the flow. In Section 5.1, we relax the assumption that the flow field is strictly irrotational, allowing for a wake behind the reed, and investigate whether the force from the acceleration is responsible for inducing the oscillations observed in real reeds. Finally, in Section 5.5, we relax the assumption that the flow rate must be constant, leading to the most plausible physical picture of reed vibration.

Chapter 4

Conformal mapping

Looked at in cross section, the reed and support plate form the boundaries of a doubly connected two-dimensional region. Recent work [21] has made it possible to find exact solutions for two dimensional potential flows in doubly connected regions. In this chapter, we use some of those techniques to solve for the flow in a two-dimensional reed and support plate system under the assumption that the flow is incompressible and irrotational.

Our first assumption is that the flow is two-dimensional. Cottingham, Lilly, and Reed have shown [16] that the motion of a free reed is described well by the first mode of oscillation of a cantilevered beam. The reed's motion can therefore be characterized by a single parameter, for example, the displacement at the tip of the reed. In Section 5.1, we show that the time evolution of this displacement is governed by a linear second-order ODE with constant coefficients, with a forcing term that is simply an appropriately weighted integral of the force along the length of the reed. We do not attempt to describe the lengthwise dependence of the force. However, if we assume the lengthwise dependence is constant, we can solve for the flow in cross section, and our calculation of the force will be correct up to some order one multiplier. In other words, we can correctly imagine the reed to be an oscillating plate in a two-dimensional flow, with the understanding that predictions of the reed's amplitude of oscillation cannot be made exactly.

A more debatable assumption is that the flow is irrotational. St. Hilaire, Wilson,

and Beavers [30] have done flow visualization studies of free reeds and concluded that a wake forms downstream of a reed, as would be expected for high Reynolds number flow past a flat plate [38]. Because the wake would be absent in potential flow, the forces on an actual free reed are possibly very different than those predicted here. Even a model that uses purely potential flow, however, may capture the oscillatory behavior.

Whether a potential flow model can produce oscillations is far from obvious at the outset. From D'Alembert's paradox [1], the force on an object in a simply-connected region of fluid is zero; this would apply to a free reed by itself, in the absence of a support plate. However, our system consists of both the reed and the support plate, which defines the second boundary in a doubly-connected region of fluid. Just as the support plate enables a real reed to oscillate, we may find that the second boundary causes our model reed to oscillate.

4.1   The reed

We describe the dynamics of the reed with a single parameter, $h(t)$, representing the height of some fixed cross-section of the reed, the tip for example, above the support plate. This height satisfies an equation of the form

$$m\ddot{h} + m\omega_0^2(h - h_0) = -F(h, \dot{h}),$$

which we will show rigorously in Section 5.1. Here, h_0 is the reed's initial (unforced) height, m its mass per unit length, ω_0 its natural frequency, and F the fluid force (drag) per unit length, which we will see depends on both the reed's current height and its velocity. The width of the slot in the support plate, W, does not appear in this equation, but will be important in the calculation of the flow. For a particular free reed, measured values for these quantities are $h_0 \approx 0.02\ cm$, $W \approx 0.2\ cm$, $\omega_0 \approx 5,000\ Hz$, and $m \approx 0.08\ g/cm$.

To obtain an estimate for the flow rate past the reed, we apply the steady Bernoulli

40

formula to a streamline originating far upstream, where the pressure is held fixed at some value Δp above atmospheric, and ending in the jet through the gap between the reed and the support plate, where the pressure is atmospheric. Using the reed's equilibrium height to calculate the area of the gap, the formula gives

$$\Delta p = \frac{1}{2}\rho \left(\frac{Q}{h_0}\right)^2 .$$

Using a typical driving pressure of $\Delta p \approx 2\ kPa$, the area flow rate Q is approximately $100\ cm^2/s$.

We scale all lengths by W, time by $1/\omega_0$, and mass by mW. (The influence of the length of the reed will show up in the natural frequency ω_0.) Thus, velocities are scaled by $\omega_0 W$, velocity potentials by $\omega_0 W^2$, pressures by $\omega_0^2 m$, and forces (per unit length) by $\omega_0^2 mW$. Typical values for the dimensionless quantities h_0, Δp, and Q are then $h_0 \approx 0.1$, $\Delta p \approx 0.01$, and $Q \approx 0.6$, although these of course may vary by a factor of roughly two or three, since a reed can be set at different initial heights and can be driven over a range of pressures. The equation of motion for the reed's height, written in terms of dimensionless quantities, is

$$\ddot{h} + (h - h_0) = -F(h, \dot{h}). \tag{4.1}$$

The width of the reed is fixed, and is typically slightly less than the width of the slot. Therefore the dimensionless reed width, which we call w, is slightly less than 1.

The force $F(h, \dot{h})$ will be calculated by solving for an irrotational, incompressible flow in the doubly-connected two-dimensional region bounded by the reed and the support plate. Our analysis will be quasistatic, that is, the flow field will be completely determined by the reed's current position h and velocity $\dot{h}$. The flow field we obtain will be described by a complex potential $w(z, t)$, analytic in the region except at a source and a sink which will be introduced to impose a flow of some prescribed Q past the reed.

41

4.2 Conformal map

The flow field will be solved by introducing a conformal map $z(\zeta, t)$ from the annulus $\rho < |\zeta| < 1$ in the ζ plane to the reed in the z plane defined by

$$z(\zeta, t) = A + B \int_{-\rho}^{\zeta} \frac{P(\zeta'\alpha^{-1})P(\zeta'\bar\alpha^{-1})P(\zeta'\beta^{-1})P(\zeta'\bar\beta^{-1})}{P^2(\zeta')P^2(-\zeta')} \frac{d\zeta'}{\zeta'^2}, \qquad (4.2)$$

where the parameters ρ, $\alpha = e^{ia}$, $\beta = \rho e^{ib}$, A, and B are functions of t. The special function $P(\zeta)$ is defined in equation (10) of [22],

$$P(\zeta) = (1 - \zeta) \prod_{k=1}^{\infty} (1 - \rho^{2k}\zeta)(1 - \rho^{2k}\zeta^{-1}). \qquad (4.3)$$

We truncate the infinite sum after M terms; later, we investigate how large a value of M is necessary for accurate calculations. Fig. 4-1 shows the image of the annulus under an example of this map. The image of $|\zeta| = \rho$ represents the reed and the image of $|\zeta| = 1$ represents the support plate. The points $\zeta = \pm 1$ map to infinity. As seen in this figure, we will use the convention that the reed is oriented vertically, with the oscillations occurring horizontally.

The five parameters must be chosen to give the image the desired geometry. The parameters A and B simply translate and scale the image; for values of a, b, and ρ, they can be chosen to make the slot centered on the origin and of width 1. The convention that the reed moves horizontally means that A and B will be real.

The parameters that characterize the proportions of the reed are a, b, and ρ. Both a and b are real and between 0 and π, and ρ, the radius of the inner circle in the ζ plane, is between 0 and 1. They must be chosen so that the image of the map has the desired reed height $h(t)$ and reed width w. In addition, the map must be single-valued throughout the annulus; that is, the function

$$c(\alpha, \beta, \rho) = \oint_{|\zeta'|=\rho} \frac{P(\zeta'\alpha^{-1})P(\zeta'\bar\alpha^{-1})P(\zeta'\beta^{-1})P(\zeta'\bar\beta^{-1})}{P^2(\zeta')P^2(-\zeta')} \frac{d\zeta'}{\zeta'^2}$$

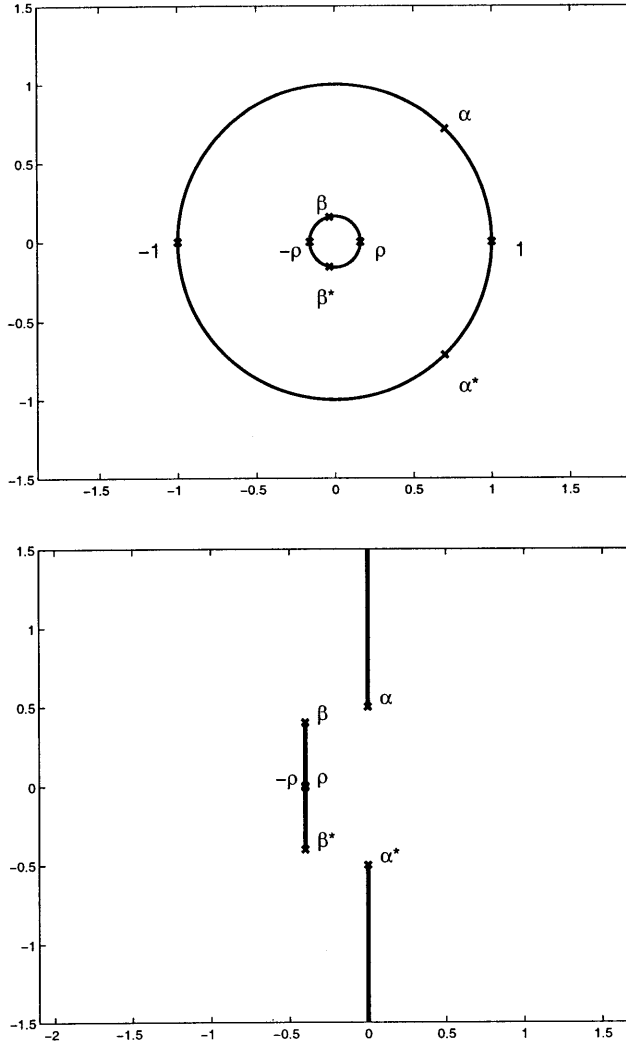must evaluate to zero. For given $h(t)$ and w, we use the Newton-Raphson method

Figure 4-1: The $|\zeta| = 1$ and $|\zeta| = \rho$ circles in the ζ plane (top), and their images (bottom) under the map defined in Eq. (4.2) with $a \approx 0.80$, $b \approx 1.80$, $\rho \approx 0.16$, $A \approx -0.40$, and $B \approx 0.03$. The image of $|\zeta| = 1$ is the vertical line whose real coordinate is 0 with a gap between $-0.5i$ and $0.5i$; this represents the support plate. The image of $|\zeta| = \rho$ is the single vertical line to the left, which represents the reed itself. The images of the points α and β, and their complex conjugates, are marked, as well as the images of $\pm\rho$. The points ± 1 map to infinity. In our setup, the reed moves horizontally, with $-h(t)$ measuring the reed's location on the real line.

43

[28] to find the values of a, b, and ρ that satisfy

$$h(a, b, \rho) = h(t)$$

$$w(a, b, \rho) = w$$

$$c(a, b, \rho) = 0.$$

In order to evaluate the pressure, it will be necessary to calculate the time derivatives of certain functions, for example, the complex potential. However, these functions are not explicit functions of time; rather, they are calculated from the values of the map parameters a, b, ρ, A, and B, which change in time as the reed moves in the physical plane. We require a way to calculate these time derivatives from the time dependence of the physical variables.

Since A and B are calculated from values of a, b, and ρ, the functions can be regarded as functions of a, b, and ρ only, the latter being functions of time. (They may also depend on ζ, but this dependence will be suppressed in the notation here.) By the chain rule, the time derivative of any such function $f(a, b, \rho)$ can be calculated from the time derivatives of the map parameters $a(t)$, $b(t)$, and $\rho(t)$,

$$\frac{df}{dt} = \frac{\partial f}{\partial a}\frac{da}{dt} + \frac{\partial f}{\partial b}\frac{db}{dt} + \frac{\partial f}{\partial \rho}\frac{d\rho}{dt}.$$

The quantities $\partial f / \partial a$, etc., which indicate how the function is affected by varying the map parameters, can be calculated numerically, for example,

$$\frac{\partial f}{\partial a}(a, b, \rho) = \frac{f(a + da, b, \rho) - f(a, b, \rho)}{da}.$$

We also need to calculate how the map parameters change with time, da/dt, etc. As the reed moves, the map parameters a, b, and ρ must change together in such a way as to change the reed's height $h(a, b, \rho)$ appropriately, while keeping the reed's width $w(a, b, \rho)$ fixed at w and the value of $c(a, b, \rho)$ fixed at zero,

$$h(t) = h(a, b, \rho)$$

44

$$w = w(a, b, \rho)$$

$$0 = c(a, b, \rho).$$

Taking the total time derivative of these equations gives

$$\frac{dh}{dt} = \frac{\partial h}{\partial a}\frac{da}{dt} + \frac{\partial h}{\partial b}\frac{db}{dt} + \frac{\partial h}{\partial \rho}\frac{d\rho}{dt}$$

$$0 = \frac{\partial w}{\partial a}\frac{da}{dt} + \frac{\partial w}{\partial b}\frac{db}{dt} + \frac{\partial w}{\partial \rho}\frac{d\rho}{dt}$$

$$0 = \frac{\partial c}{\partial a}\frac{da}{dt} + \frac{\partial c}{\partial b}\frac{db}{dt} + \frac{\partial c}{\partial \rho}\frac{d\rho}{dt}.$$

When the velocity of the reed dh/dt is specified, this linear system of equations can be solved for da/dt, db/dt, and $d\rho/dt$. We calculate the quantities $\partial h/\partial a$, etc., numerically, for example,

$$\frac{\partial h}{\partial a}(a, b, \rho) = \frac{h(a + da, b, \rho) - h(a, b, \rho)}{da}.$$

4.3 Complex potential

With the reed's current configuration specified, we turn to the problem of describing the flow. From a complex potential $w(z)$, the velocity field, and in turn the pressure field, can be calculated. We seek to solve the problem in the annulus $\rho < |\zeta| < 1$ rather than in the physical plane, and so introduce the complex potential in the zeta plane, $W(\zeta) = w(z(\zeta))$.

Because the reed is moving, the normal component of the fluid velocity at the boundaries must match the velocity of each boundary. The complex potential must be chosen appropriately. Crowdy, Surana, and Yick [22] show that when the boundary conditions are written as conditions on the complex potential in the ζ plane, they reduce to a version of the modified Schwarz problem. Calling this complex potential W_2 and the imposed velocities on the outer and inner boundaries U_0 and U_1, these

conditions are

$$Re\left[-iW_2(\zeta)\right] = Re\left[-i\overline{U_0}z(\zeta)\right] + d_0 \tag{4.4}$$

$$Re\left[-iW_2(\zeta)\right] = Re\left[-i\overline{U_1}z(\zeta)\right] + d_1, \tag{4.5}$$

where the first condition applies on the outer circle, $|\zeta| = 1$, and the second on the inner circle, $|\zeta| = \rho$. For clarity, constants have been retained in both conditions. Any values of these constants will satisfy the boundary conditions; however, it will be seen that the constants cannot be chosen independently if the problem is to have a solution.

We use the following procedure [18] to solve for $W_2(\zeta)$. The known expression on the right hand side of each boundary condition can be written as a Fourier series,

$$Re\left[-i\overline{U_0}z(\zeta)\right] = \sum_{n=-(K/2-1)}^{K/2-1} f_n\zeta^n$$

$$Re\left[-i\overline{U_1}z(\rho\zeta)\right] = \sum_{n=-(K/2-1)}^{K/2-1} g_n\zeta^n,$$

where the substitution $\zeta \rightarrow \rho\zeta$ has been used in the second condition so that both conditions apply on $|\zeta| = 1$. The correspondence with Fourier series can be seen by taking $\zeta = e^{i\theta}$,

$$Re\left[-i\overline{U_0}z(e^{i\theta})\right] = \sum_{n=-(K/2-1)}^{K/2-1} f_n e^{in\theta}$$

$$Re\left[-i\overline{U_1}z(\rho e^{i\theta})\right] = \sum_{n=-(K/2-1)}^{K/2-1} g_n e^{in\theta},$$

from which it is clear that the coefficients f_n and g_n for $n = -(K/2 - 1)$ through $K/2 - 1$ can be found by an FFT. The appropriate number of coefficients to use in the analysis, K, will be investigated later.

We write the unknown function $W_2(\zeta)$ as a Laurent series in the following form,

$$-iW_2(\zeta) = \sum_{n=0}^{K/2-1} a_n \zeta^n + \sum_{n=1}^{K/2-1} \rho^n a_{-n} \zeta^{-n}. \tag{4.6}$$

The factors of ρ have been introduced for numerical stability. The goal is to calculate the values of the coefficients $a_{-(K/2-1)}$ through $a_{K/2-1}$. Substituting the series into both boundary conditions, using $\overline{\zeta} = 1/\zeta$, and equating positive powers of ζ gives formulas for the coefficients,

$$a_n = \frac{2(f_n - \rho^n g_n)}{1 - \rho^{2n}}$$

$$a_{-n} = \frac{2(\overline{g_n} - \rho^n \overline{f_n})}{1 - \rho^{2n}},$$

for $n = 1$ through $K/2 - 1$. Equating the ζ^0 terms of the conditions gives two more formulas,

$$Re[a_0] = f_0 + d_0$$

$$Re[a_0] = g_0 + d_1.$$

We choose $d_0 = 0$, so that the first equation gives the real part of a_0. d_1, though not needed for the calculation, would have to be chosen to make the second equation consistent. The imaginary part of a_0 is arbitrary as well; we choose 0.

For our problem, the reed is moving and the support plate is stationary; thus $U_0 = 0$ and $U_1 = -\dot{h}$. With the coefficients of $W_2(\zeta)$ now known, it can be evaluated on $|\zeta| = \rho$ by substitution into Eq. (4.6). Likewise, $\partial W_2/\partial \zeta$ can be evaluated on $|\zeta| = \rho$ by substitution into the derivative of Eq. (4.6).

We wish to impose a uniform flow. To accomplish this, we include another contribution to the complex potential,

$$W_1(\zeta) = \frac{Q}{2\pi} \log \frac{P(\zeta c^{-1})P(\zeta \overline{c})}{P(-\zeta c^{-1})P(-\zeta \overline{c})}.$$

47

Because $P(\zeta c^{-1})$ and $P(-\zeta c^{-1})$ have zeros at $\zeta = c$ and $\zeta = -c$, respectively, $W_1(\zeta)$ has logarithmic singularities at $\zeta = c$ and $\zeta = -c$, respectively,

$$W_1(\zeta) \sim \frac{Q}{2\pi} \log(\zeta - c)$$

$$W_1(\zeta) \sim -\frac{Q}{2\pi} \log(\zeta + c).$$

$W_1(\zeta)$ thus represents a source at $z(-c)$ and a sink at $z(c)$, both of strength Q. As described later, c will be chosen so that $z(-c)$ and $z(c)$ are sufficiently far from the reed that it effectively sees a uniform flow in the far field.

The derivative $\partial W_1/\partial \zeta$ will also be required to calculate the velocity. It can be written as

$$\frac{\partial W_1}{\partial \zeta} = \frac{Q}{2\pi\zeta} \left(K(\zeta c^{-1}) + K(\zeta \bar{c}) - K(-\zeta c^{-1}) - K(-\zeta \bar{c}) \right). \tag{4.7}$$

$K(\zeta)$ is a special function defined in equation (40) of [20],

$$K(\zeta) = \frac{\zeta P'(\zeta)}{P(\zeta)}$$

$$= \zeta \left(-\frac{1}{1-\zeta} - \sum_{k=1}^{M} \frac{\rho^{2k}}{1-\rho^{2k}\zeta} + \sum_{k=1}^{M} \frac{\rho^{2k}\zeta^{-2}}{1-\rho^{2k}\zeta^{-1}} \right)$$

For the total complex potential $W(\zeta)$, we use the sum of the two contributions, $W(\zeta) = W_1(\zeta) + W_2(\zeta)$. It can be shown that the imaginary part of $W_1(\zeta)$ is constant on both boundaries. Using this, it can be verified by substitution that the total complex potential $W(\zeta)$ satisfies the same boundary conditions as $W_2(\zeta)$, Eq. (4.4-4.5), for possibly different constants.

Fig. 4-2 shows the fluid velocity field for a particular reed geometry and velocity.
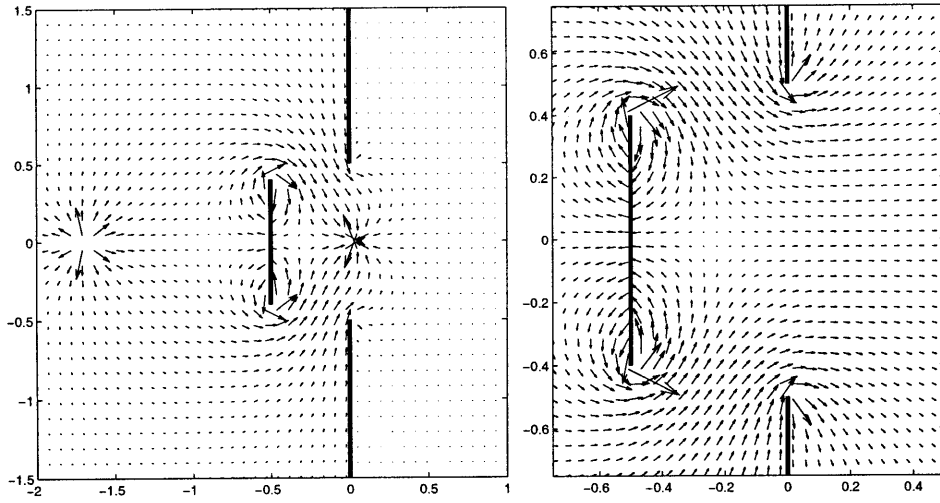
Figure 4-2: Left: The velocity field for a reed with width $w = 0.8$ and height $h = 0.5$, moving at velocity $\dot{h} = 0.5$, with flow rate $Q = 0.5$. $c = -0.5$ has been chosen for the source/sink position in the ζ plane in order to show the source and sink in the plot. Right: Closeup of the velocity field for the same parameters, except with $c = -0.999$, to simulate uniform flow in the far field. This larger value of c is used for the actual calculations. The magnitude of the arrows is arbitrary in both plots.

4.4 Force on the reed

With the reed geometry $z(\zeta, t)$ and the flow field $W(\zeta, t) = w(z(\zeta, t), t)$ known, the force on the reed can be calculated.

The pressure at any point in the flow satisfies the unsteady Bernoulli formula,

$$\frac{\partial \phi}{\partial t} + \frac{1}{2}u^2 + \frac{p}{\rho} = G(t), \qquad (4.8)$$

where $G(t)$ is an arbitrary function of time whose value turns out to be unimportant for the total force. Written in terms of dimensionless quantities, this formula may be reexpressed as

$$\frac{\partial \phi}{\partial t} + \frac{1}{2}u^2 + \frac{p}{\rho_d} = G(t),$$

where ρ_d is the dimensionless fluid density,

$$\rho_d = \frac{\rho W^2}{m}.$$

49

For our reed in air, the value of this parameter is approximately $\rho_d \approx 5 \times 10^{-4}$.

Expressed in terms of the complex potential $w = \phi + i\psi$, where $\bar{u} = \partial w / \partial z$, the formula is

$$Re\frac{\partial w}{\partial t} + \frac{1}{2}\left|\frac{\partial w}{\partial z}\right|^2 + \frac{p}{\rho_d} = G(t).$$

Using the unit normal $n = -idz/ds$, the total force $F_x + iF_y$ is the following integral around the boundary of the object in the z plane,

$$-\oint pn \, ds = i \oint p \, dz,$$

with p/ρ_d given in terms of $\partial w/\partial z$ and $\partial w/\partial t$ above, and $G(t)$ dropping out of the final integral.

We need to write $\partial w/\partial z$ and $\partial w/\partial t$, the derivatives of the complex potential in the physical plane, in terms of $\partial z/\partial\zeta$, $\partial z/\partial t$, $\partial W/\partial\zeta$, and $\partial W/\partial t$, the derivatives of the map and potential in the ζ plane. Using the definition of $W(\zeta, t)$,

$$W(\zeta, t) = w(z(\zeta, t), t),$$

these relationships follow from the chain rule,

$$\frac{\partial W}{\partial\zeta} = \frac{\partial w}{\partial z}\frac{\partial z}{\partial\zeta}$$

$$\frac{\partial W}{\partial t} = \frac{\partial w}{\partial z}\frac{\partial z}{\partial t} + \frac{\partial w}{\partial t}.$$

Therefore $\partial w/\partial z$ and $\partial w/\partial t$ are given by

$$\frac{\partial w}{\partial z} = \frac{\partial W}{\partial\zeta}\bigg/\frac{\partial z}{\partial\zeta}$$

$$\frac{\partial w}{\partial t} = \frac{\partial W}{\partial t} - \left(\frac{\partial W}{\partial\zeta}\bigg/\frac{\partial z}{\partial\zeta}\right)\frac{\partial z}{\partial t}.$$

Putting everything together, and using $dz = (\partial z/\partial\zeta)d\zeta$, the complex force $F_x + iF_y$

50

is given by

$$F = -\frac{1}{2}i\rho_d \oint_{|\zeta|=\rho} \left(\frac{\partial W}{\partial t}\frac{\partial z}{\partial \zeta} + \frac{\overline{\partial W}}{\partial t}\frac{\partial z}{\partial \zeta} - \frac{\partial W}{\partial \zeta}\frac{\partial z}{\partial t} - \frac{\overline{\partial W}}{\partial \zeta}\frac{\overline{\partial z}}{\partial t}\frac{\partial z}{\partial \zeta}\bigg/\frac{\overline{\partial z}}{\partial \zeta} + \frac{\partial W}{\partial \zeta}\frac{\overline{\partial W}}{\partial \zeta}\bigg/\frac{\overline{\partial z}}{\partial \zeta} \right) d\zeta$$

The fourth and fifth terms have singularities at $\zeta = \beta$ and $\zeta = \overline{\beta}$, the points that map to the ends of the reed. Physically, this is because our potential flow model requires the fluid to turn $180°$ there, causing its velocity to be undefined. This happens because the tangent to the reed, $dz/d\zeta$, is zero at those points. By inspection of Eq. (4.2), $dz/d\zeta$ has a simple zero at β and $\overline{\beta}$; therefore the conjugates of the integrals of the fourth and fifth terms can be calculated using the Plemelj formula. Using the relation $\zeta\overline{\zeta} = \rho^2$ on the $|\zeta| = \rho$ circle, the conjugates of those integrals are, respectively,

$$\oint_{|\zeta|=\rho} \frac{\partial W}{\partial \zeta}\frac{\partial z}{\partial t}\frac{\overline{\partial z}}{\partial \zeta}\bigg/\frac{\partial z}{\partial \zeta}\frac{\rho^2}{\zeta^2}\, d\zeta \quad,$$

$$-\oint_{|\zeta|=\rho} \frac{\overline{\partial W}}{\partial \zeta}\frac{\partial W}{\partial \zeta}\bigg/\frac{\partial z}{\partial \zeta}\frac{\rho^2}{\zeta^2}\, d\zeta \quad.$$

The Plemelj formula give, for functions $f(\zeta)$ with simple zeros at β and $\overline{\beta}$,

$$\oint_{|\zeta|=\rho} f(\zeta)\, d\zeta = \pi i \left(Res(f,\beta) + Res(f,\overline{\beta}) \right) + P.V. \oint_{|\zeta|=\rho} f(\zeta)\, d\zeta.$$

We calculate $Res(f,\beta)$ numerically, by evaluating

$$Res(f,\beta) = (\zeta - \beta)f(\zeta)$$

for a small value of $\zeta - \beta$. We calculate the principal value integral using the alternate-point trapezoidal rule [18].

Due to the vertical symmetry of the problem, we expect the imaginary part of F to be zero to within numerical error. The real part turns out to be fairly small compared to the other quantities, on the order of 10^{-6}. We expect the fluid force to be much smaller than the elastic force, because the reed undergoes fixed-amplitude oscillations on a short time scale, requiring a long time scale (hundreds of oscillations) for the fluid force to appreciably change the amplitude.
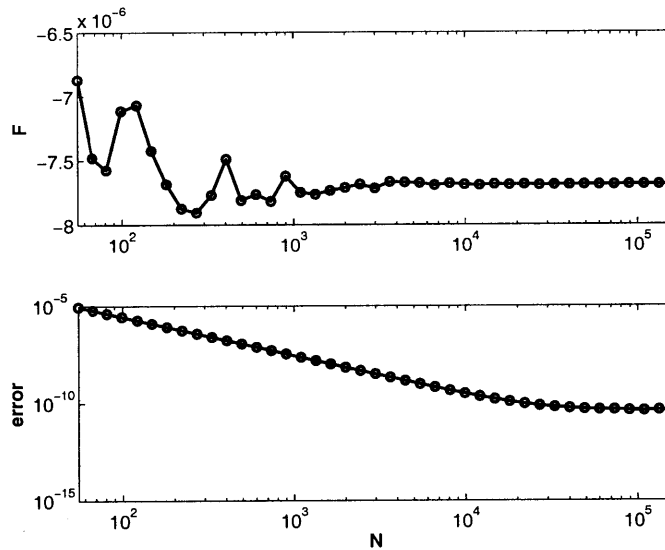
51

Figure 4-3: Real part of force (upper plot) and numerical error in the boundary condition on the inner circle, Eq. (4.5), (lower plot) as the number of integration points N is increased. The error in the boundary condition on the outer circle is always much lower. For this and subsequent convergence tests, we use values for the parameters obtained from the other convergence tests, $M = 10$, $K = 30$, and $c = -0.999$. We use a reed with geometry $w = 0.8$, $h = 0.5$, $\dot{h} = 0.5$, and $Q = 0.5$.

4.5 Convergence tests

In this section, we justify our choice of values for the numerical resolutions N, K, and M, and the location of the source and sink, c. We also check that our calculation satisfies D'Alembert's paradox when the reed and support plate are sufficiently far away.

In order to determine how many integration points are necessary to use for the calculations, we analyze the convergence of the force F, as well as the discrepancy in the boundary conditions, Eq. (4.4-4.5), as N is increased. From these results, shown in Fig. 4-3, we choose $N = 1000$, which appears to give an accuracy of about 1%. We use this value in all calculations, unless otherwise stated. To determine how many coefficients K are necessary for the Fourier series used for the calculation of W_2, we plot the convergence as K is increased in Fig. 4-4. We choose $K = 30$ for our calculations, by which point the force has converged to its final value to within a factor of 2×10^{-8}. Finally, to determine how many terms are necessary to include in
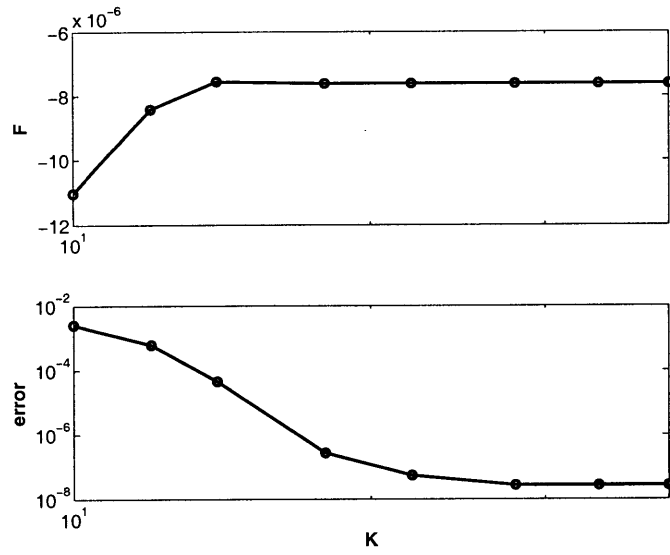
Figure 4-4: Real part of force (top) and error in the inner boundary condition (bottom) as K varies, for the same parameters as in Fig. 4-3.
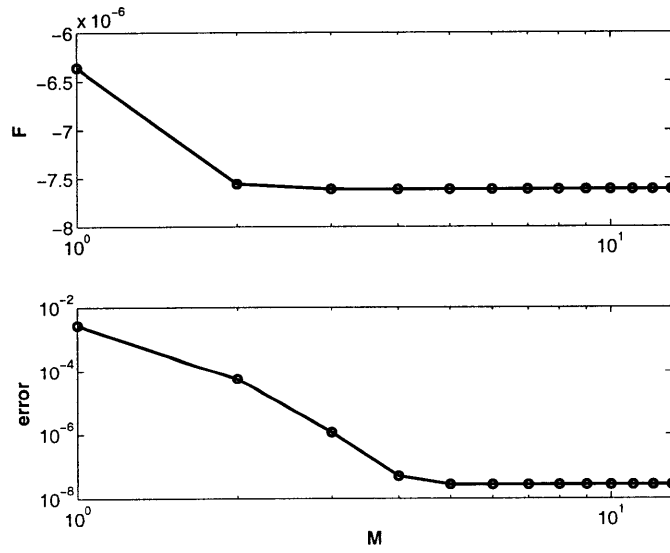

Figure 4-5: Real part of force (top) and error in the inner boundary condition (bottom) as M varies, for the same parameters as in Fig. 4-3.
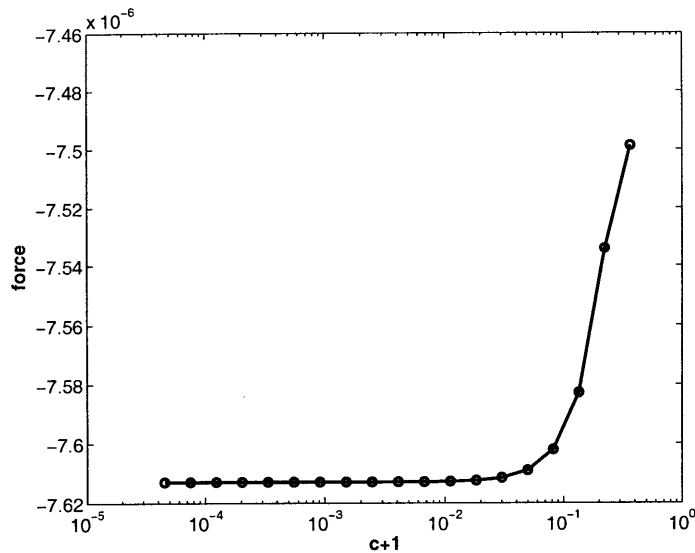
Figure 4-6: Plot of the force as the value of c in Eq. (4.7) is varied. The x axis indicates how far c is from $\zeta = -1$.

the evaluation of $P(\zeta)$ in Eq. (4.3), we plot the convergence as M is increased in Fig. 4-5. We choose $M = 10$, by which point the force has converged to its final value to within a factor of 5×10^{-7}.

As described above, the complex potential includes terms for a source and sink located at c and $-c$, respectively, in the ζ plane, where c is a negative real number. The value of c must be chosen so that the points $z(\pm c)$ are far enough from the reed that it effectively sees a uniform flow. This occurs when c is close to the outer boundary of the annulus, near $\zeta = -1$, which maps to infinity in the z plane. In order to investigate how close c must be to -1, we calculate the force as c is varied. The results are shown in Fig. 4-6. The force rapidly converges as c converges to -1; after $c = -0.999$, for example, it has converged to its final value to within a factor of 10^{-6}. We use this value, $c = -0.999$, in calculations.

In the absence of a support plate, the reed, like any object in a simply-connected flow region, should feel no force. Therefore, as a check on the calculation, the force should tend towards zero as the reed is positioned farther from the plate. Fig. 4-7 confirms this.
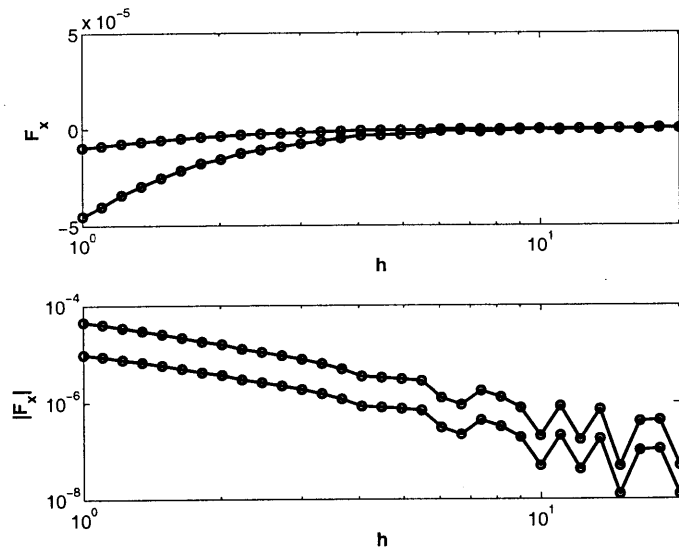
54

Figure 4-7: Plots of the real part of the force on the reed as h is varied: log-linear plot above; log-log plot below. The curve with smaller absolute value is for $\dot{h} = 0.5$, the one with larger absolute value, $\dot{h} = 1$.

4.6 Motion of the reed

Now that we are able to calculate the fluid force $F(h, \dot{h})$, we can use Eq. (4.1) to analyze the motion of the reed. We perform a linear stability analysis to investigate the parameters for which reed oscillation is possible. The equilibrium position can be calculated by substituting $h = h^*$, $\dot{h} = \ddot{h} = 0$ into Eq. (4.1),

$$h^* - h_0 = -F(h^*, 0), \tag{4.9}$$

and solving for h^*. In the analysis that follows, we treat the equilibrium position h^* as given. The initial position h_0 for which h^* is the equilibrium could be calculated by solving Eq. (4.9), if desired.

The stability of an equilibrium position h^* can be determined by linearizing Eq. (4.1) around $h = h^*$, $\dot{h} = 0$. Near this equilibrium, the fluid force can be approximated by

$$F(h, \dot{h}) \approx F(h^*, 0) + \frac{\partial F}{\partial h}(h^*, 0)(h - h^*) + \frac{\partial F}{\partial \dot{h}}(h^*, 0)\dot{h}.$$

Using $u = h - h^*$ and $v = \dot{h}$ to measure the perturbation of the position and velocity from the equilibrium, Eq. (4.1) can be converted into a linear system for these quantities,

$$\dot{u} = v$$
$$\dot{v} = -(1 + F_h)u - F_{\dot{h}}v$$

Here, F_h and $F_{\dot{h}}$ are used as shorthand for $\partial F/\partial h(h^*, 0)$ and $\partial F/\partial \dot{h}(h^*, 0)$, the corresponding partial derivatives evaluated at the equilibrium point with $\dot{h} = 0$; we calculate these derivatives numerically. The eigenvalues of the matrix for this system are

$$\lambda = \frac{-F_{\dot{h}} \pm \sqrt{F_{\dot{h}}^2 - 4(1 + F_h)}}{2}.$$

When $F_{\dot{h}}^2 < 4(1 + F_h)$, the eigenvalues are complex, so the linear system exhibits oscillations. These oscillations are unstable when the real part of the eigenvalues,

$$Re[\lambda] = -F_{\dot{h}} \tag{4.10}$$

is positive.

The goal is to determine the conditions under which the reed can be induced to oscillate, that is, when the eigenvalues are complex with positive real part. We choose values for the reed width and flow rate and calculate the eigenvalues over a range of h^*. We find that they are always complex. The real part of the eigenvalues for a few different reed widths is plotted in Fig. 4-8. Positive values indicate that the flow will induce oscillations; negative values indicate that oscillations will be damped. Evidently, if the reed is very close to the support plate, no oscillations occur. However, there seems to be a critical distance above which the reed does oscillate, although the growth rate of the oscillations diminishes for large h^*. This is the opposite of the behavior that is observed for actual reeds, which must be positioned close to the support plate in order to work. Evidently the potential flow calculation predicts different behavior than is observed for real reeds.
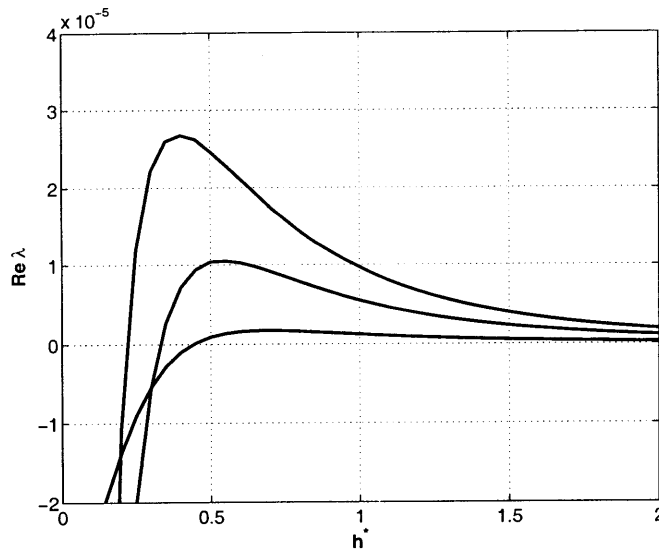
Figure 4-8: $Re[\lambda]$, calculated according to Eq. (4.10), as the equilibrium position h^* is varied, with flow rate $Q = 1$. For this range of h^*, the eigenvalues are always complex, so the real parts of both eigenvalues are equal. Each curve is for a different reed width: From top to bottom, $w = 0.95$, 0.8, and 0.5. The model predicts that the reed will oscillate when h^* is above some critical value which decreases as the reed width approaches the width of the slot.

Fig. 4-8 also shows that the growth rate depends on the reed geometry. For reeds whose width is almost that of the slot in the support plate, the growth rate is rapid; the growth is diminished if the reed is made significantly smaller than the slot. In addition, reeds that are almost as wide as the slot will oscillate over a greater range of h^* than reeds with more clearance. This agrees with the behavior of actual free reeds, which are usually manufactured with close tolerances. Anecdotally, if there is a lot of extra clearance between the edge of the reed and the support plate, the reed is less responsive.

It is worth noting that it is vital to include the time-dependent terms in the formula for the pressure, the terms that come from the first term in Eq. (4.8). Fig. 4-9 compares the linear stability calculation performed with and without these terms. Physically, if the time-dependent terms are absent, the only variation in the force that comes from varying $\dot{h}$ comes from the fluid that must be displaced by the moving reed; the fact that the gap size varies in time, changing the flow rate, is not taken into account. Including the time-dependent terms is what allows the steady
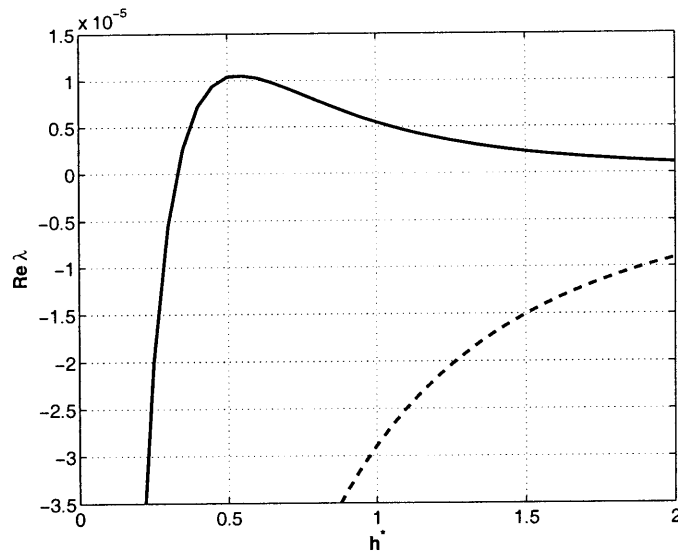
57

Figure 4-9: $Re[\lambda]$ versus h^*, plotted with (solid) and without (dashed) the time-dependent terms, the first term in Eq. (4.8), for $w = 0.8$ and $Q = 1$.

imposed flow to drive the reed.

Fig. 4-10 shows the effect of changing the flow rate on the growth rate. As expected, when the flow rate is larger, which corresponds to the reed being driven at a higher pressure, the growth rate is larger. Interestingly, when the flow rate is negative, corresponding to the reed being driven in the other direction, the reed behaves differently: A reed close to the support plate is induced to oscillate, while a reed far away is not. This is not consistent with the behavior of real free reeds driven in the wrong direction, which do not oscillate at all. Instead, it is closer to the behavior of real free reeds driven in the proper direction. The characteristic behavior of free reeds evidently depends on the non-ideal nature of the flow.

In conclusion, this theory captures certain aspects of the problem: A steady flow can induce oscillations of a reed by virtue of the doubly-connected reed-plate geometry. This model agrees with actual free reeds in that oscillation is made easier by a reed positioned closer to the support plate, a smaller clearance between the reed and the edge of the support plate, and a larger flow rate. It fails to capture the fact that a reed only oscillates when positioned very close to its support plate on the upstream side. Most likely, the failure stems from the inability of a potential flow theory to
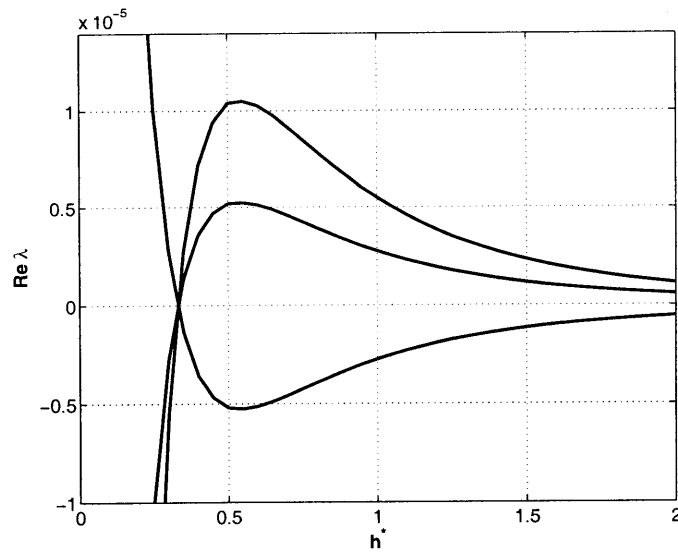
Figure 4-10: $Re[\lambda]$ versus h^*, plotted for different flow rates Q: From top to bottom, $Q = 1$, 0.5, and -0.5. In this plot, the reed width is fixed at $w = 0.8$.

take into account the wake behind the reed. These results do offer insight on how to proceed next: It is evidently important to take into account the time-dependent term in the Bernoulli formula. Physically, this term represents the force on the reed resulting from acceleration of the fluid. In our next model, we retain this feature of the current model but propose a more realistic description of the flow.

Chapter 5

Further theoretical modeling

In the previous chapter, we solved for the flow field under several assumptions, the most significant being that the flow is irrotational. This model failed to make qualitatively correct predictions of the conditions under which a free reed will oscillate, a discrepancy most likely due to the fact that a potential flow model fails to take into account the presence of a wake behind the reed, as was observed by St. Hilaire, Wilson, and Beavers [30]. The analysis did indicate the importance of the time-dependent term in the Bernoulli formula, which represents the force on the reed due to the acceleration of the flow. In light of these results, we proceed by constructing a theory that incorporates both this acceleration and the wake behind the reed.

5.1   Vibration of beams

Before describing the flow model, we will first improve upon our earlier description of a reed as a rigid plate, instead treating the reed as a flexible beam. This will enable our predictions to be compared with measurements for an actual reed.

Rayleigh [44] gives the equation of motion for lateral vibrations of a beam with rectangular cross section. In our notation, described in Table 3.1, this equation is

$$\rho_r h W y_{tt} + \frac{1}{12} h^3 W E y_{xxxx} = F(x,t),$$

where $y(x,t)$ is the lateral displacement of the beam and $F(x,t)$ is an externally imposed force per unit length. x indicates the position along the beam from 0 to L and t indicates time. We assume that $h \ll W \ll L$, which is largely true for real reeds. Here, the beam is fixed at $x = 0$ and free at $x = L$.

Previous work [16] indicates that the shape of a free reed during oscillation is described well by the shape of the first mode of an unforced beam. The mode shapes can be found by looking for solutions of the homogeneous equation with a sinusoidal time dependence,

$$y(x,t) = f(x) \, cos \left(\frac{m^2}{\sqrt{12}} \frac{h}{L^2} \sqrt{\frac{E}{\rho_r}} \, t \right),$$

requiring the mode shape $f(x)$ to satisfy the equation

$$f_{xxxx} = \frac{m^4}{L^4} f.$$

Rayleigh gives the solutions,

$$
\begin{aligned}
f_m(x) \;=\; & (sin \; m + sinh \; m) \left(cos \, \frac{mx}{L} - cosh \, \frac{mx}{L} \right) \\
& -(cos \; m + cosh \; m) \left(sin \, \frac{mx}{L} - sinh \, \frac{mx}{L} \right),
\end{aligned}
$$

with $m = m_1 = 1.875104$ corresponding to the first mode, and shows that different mode shapes are orthogonal, in that an appropriately weighted integral of the product of two mode shapes gives zero. For convenience, $f_m(x)$ will refer to the mode shapes normalized so that $f(L) = 1$; $f(x)$ will refer to the first mode shape. It will be necessary to use the values of the integrals

$$
\begin{aligned}
F_1 \;&=\; \int_0^L f(x) \, dx \\
F_2 \;&=\; \int_0^L f^2(x) \, dx,
\end{aligned}
$$

etc., constants that can be easily computed numerically.

In order to determine the effect of an arbitrary force distribution $F(x,t)$ on the

reed, the displacement can be written as a sum of all the modes,

$$y(x,t) = \sum_m a_m(t) f_m(x).$$

Substituting into the equation of motion, multiplying by $f(x)$, and integrating from $x = 0$ to $x = L$ gives an ODE for $a_{m_1}(t)$, written henceforth as $a(t)$:

$$\rho_r h W \ddot{a} + \frac{1}{12} h^3 W E \frac{m_1^4}{L^4} a = \frac{1}{F_2} \int F(x,t) f(x) \, dx. \qquad (5.1)$$

This is an ODE for the amplitude $a(t)$ of the first mode. We neglect the presence of the other modes. Because $f(L) = 1$, $a(t)$ is just the displacement of the tip of the reed. (We will use the convention that a positive $a(t)$ is a displacement in the upstream direction.) The ODE shows that the effect of any force distribution $F(x,t)$ on the tip displacement can be found by integrating its product with the first mode shape.

5.2 Force on the reed

We wish to improve on our earlier model by accounting for the wake behind the reed. We make use of extensive studies of the flow past a flat plate. Milne-Thomson [38] presents solutions of the flow field around obstacles of a variety of geometries, including a flat plate, under the assumption that a wake is formed behind the obstacle. These solutions are presented for the case of a steady far-field velocity U. Anticipating that the unsteadiness of the velocity may be important for our problem, we extend Milne-Thomson's result for a flat plate to the case of an unsteady far-field velocity $U(t)$. As in Chapter 4, we assume that the flow adjusts instantaneously to changes in $U(t)$, that is, that the flow is always identical to the steady flow past a flat plate with the current far-field velocity. This assumption will prevent us from capturing unsteady structures in the flow, such as vortex shedding. However, as discussed in Section 3.4, the work of St. Hilaire et al. [30] suggests that a quasistatic model may be sufficient for this problem.

Milne-Thomson calculates the drag on a flat plate in a steady flow of speed U by introducing a conformal map $z(\zeta)$ from the interval $[-1, 1]$ in the ζ-plane to the plate in the z-plane. Here we use this map but allow the far-field velocity to be a function of time, $U(t)$. The complete reed-plate geometry, which we study in Section 5.3, will determine the time dependence. Using l for the width of the plate and $U(t)$ for the far field velocity (also the velocity at the edge of the plate), the conformal map is defined by equation (3) of 12.20,

$$U \frac{dz}{d\zeta} = K(-1 - \sqrt{1 - \zeta^2}),$$

where the constant K is determined from equation (4),

$$Ul = -K(2 + \pi/2).$$

He also gives the complex potential in the ζ-plane in equation (5),

$$W(\zeta) = \frac{Ul\zeta^2}{\pi + 4}.$$

Here, we change the notation to be consistent with that used in Chapter 4, and correct the sign to account for Milne-Thomson's opposite sign convention for the potential.

The pressure p at any point on the plate can be calculated by applying the time-dependent Bernoulli formula to that point and the plate's edge,

$$\frac{p}{\rho} + \frac{u^2}{2} + \frac{\partial \phi}{\partial t} = \frac{p_{edge}}{\rho} + \frac{U^2}{2} + \frac{\partial \phi_{edge}}{\partial t}.$$

The total drag (per unit length) is calculated by integrating the pressure over the plate. We follow Milne-Thomson in taking the pressure in the wake to be the pressure at the edge of the plate. The drag is then

$$D = \int (p - p_{edge}) dx = \rho \int \left(\frac{U^2}{2} - \frac{u^2}{2} + \frac{\partial \phi_{edge}}{\partial t} - \frac{\partial \phi}{\partial t} \right) dx,$$

where the integral is taken over the upper surface of the plate. It can be evaluated in

63

the ζ plane using the standard formulae for complex potential flow, $\bar{u} = dw/dz$, $\phi = Re(w)$. (The integration is trivial for the first and third terms, which are constant.) For our time-dependent potential,

$$\frac{\partial W}{\partial t} = \frac{\dot{U}l\zeta^2}{\pi + 4},$$

since the fluid velocity changes as the reed moves.

After integration, the drag on the plate (per unit length) is found to be

$$D = C_1 \rho l U^2 + C_2 \rho l^2 \dot{U}, \qquad (5.2)$$

where the constants C_1 and C_2 are

$$
\begin{aligned}
C_1 &= \quad \pi/(\pi + 4) \quad &\approx 0.44 \\
C_2 &= \quad (9\pi + 32)/(12(\pi + 4)^2) \quad &\approx 0.10.
\end{aligned}
$$

The first term is the drag on a flat plate in steady flow, while the second term is additional drag due to acceleration of the fluid; it can be regarded as the added mass of the plate. We expect the drag coefficients C_1 and C_2 to depend on a variety of factors, such as the material of the plate, but we use these calculated values for simplicity. We will apply this formula to calculate the force on a reed; the time dependence in the far field velocity will come from the effect of the support plate on the flow.

5.3   Motion of the reed

Equipped with a formula for the force on the reed in a time-dependent flow, we proceed to use the system's geometry to relate the flow to the reed's position. The essential idea we use is that the velocity is given by mass conservation: The closer the reed is to the support plate (that is, the smaller the area of the gap between the reed and the support plate), the faster the fluid must move in order to maintain a

constant flow rate. Put another way, the effect of the support plate is to control the fluid velocity.

Based on the results of the last section, we can predict how this variation in velocity affects the force on the reed. When the reed is moving away from the support plate, the size of the gap is increasing, so by mass conservation, the fluid velocity is decreasing. This makes for a smaller pressure drop across the reed, and therefore the drag is lower than if the reed were not moving. In contrast, when the reed is moving downward, the gap is getting smaller, so the fluid velocity is increasing, resulting in a larger pressure drop and therefore a larger drag. In either case, there is a force in the direction of the reed's motion in the same direction as the reed's velocity, which causes oscillations to increase in amplitude.

In order to calculate the gap area, we begin by specifying the initial shape of the reed. We allow the reed to be initially bent into some shape $q(x)$, so that the reed's shape at any time is given by

$$y(x,t) = q(x) + a(t)f(x).$$

Define a function $A(a)$ to be the area of the gap as a function of the reed tip displacement. This function describes how the gap area changes as the reed moves. If the support plate is thick enough that the reed tip never reaches below the bottom, the area function can be calculated via

$$A(a) = B + 2\int_0^L \left[q(x) + af(x)\right] \, dx + W\left[q(L) + a\right],$$

where the brackets indicate that zero should be taken when the argument is negative. Here, we have taken into account the clearance between the reed and the support plate by including a constant minimum area B. The second and third terms are the areas of the gaps at the sides and at the end of the reed, respectively. This formula only describes a reed attached to the top of its support plate. For a reed attached to the bottom, the area would instead decrease as the tip rose.

In this work, we take the reed's initial shape to be simply a multiple a_0 of the first

65

mode shape,

$$y(x, t) = (a_0 + a(t))f(x).$$

This simplifies the analysis because the reed's initial position can be described by a single parameter. It is qualitatively correct in that the height above the support plate increases towards the tip of the reed. With this simplification, the area function can be written in terms of several known constants,

$$A(a) = B + (2F_1 + W)[a_0 + a]. \tag{5.3}$$

The derivative of the area $A'(a)$ will also be needed,

$$A'(a) = 2F_1 + W, \tag{5.4}$$

or $A'(a) = 0$ when $a_0 + a < 0$.

We expect the aerodynamic force on the reed to have two contributions, one of the form for a steadily translating plate and one resulting from the unsteady nature of the flow. Using W for the width of the reed, $u_{rel}(x, t)$ for the velocity of the fluid relative to the reed, and $\sigma(x, t)$ for its sign ($+1$ or -1), Eq. (5.2) gives the force per unit length on a segment of the reed,

$$F(x, t) = \sigma C_1 \rho W u_{rel}^2 + C_2 \rho W^2 (u_{rel})_t. \tag{5.5}$$

Determining the form of u_{rel} requires that we make an assumption about the velocity distribution of the flow around the reed. The simplest model would be a uniform velocity, the velocity at every position being the flow rate $Q(t)$ divided by the area of the gap,

$$u_{fluid}(x, t) = -\frac{Q(t)}{A(a(t))}.$$

The velocity of the reed itself is a function of position,

$$u_{reed}(x, t) = a_t(t)f(x).$$

66

The relative velocity is the difference,

$$u_{rel}(x, t) = u_{fluid}(x, t) - u_{reed}(x, t). \tag{5.6}$$

Using this velocity, the fluid force on the reed can now be calculated. Substituting Eq. (5.6) into Eq. (5.5), and in turn into Eq. (5.1), gives a second-order ODE for the reed tip displacement $a(t)$,

$$\rho_r h \ddot{a} + \frac{1}{12} h^3 E \frac{m_1^4}{L^4} a = \frac{\sigma C_1 \rho}{F_2} \left(F_1 \frac{Q^2}{A^2} + 2F_2 \frac{Q}{A} \dot{a} + F_3 \dot{a}^2 \right) + \frac{C_2 \rho W}{F_2} \left(-F_1 \frac{\dot{Q}}{A} + F_1 \frac{QA'}{A^2} \dot{a} - F_2 \ddot{a} \right), \tag{5.7}$$

where for simplicity we evaluate the sign of the velocity σ at the reed tip, $\sigma(x, t) = \sigma(L, t)$. This simplification is correct as long as the flow speed exceeds the speed of the reed tip.

5.4 Constant-flow-rate theory

The ODE for $a(t)$ is not complete until a flow rate $Q(t)$ is specified. In this section, we make the assumption that $Q(t)$ is a constant; we will revisit this assumption in Section 5.5. Here, we express the flow rate Q in terms of the driving pressure Δp by the steady Bernoulli formula applied at the reed's equilibrium position. Using A^* for the reed's equilibrium area, which is approximately equal to 0.05 cm^2 for our reed, this formula is

$$\Delta p = \frac{1}{2} \rho \left(\frac{Q}{A^*} \right)^2. \tag{5.8}$$

Equations (5.3), (5.7), and (5.8) together constitute this second-order model. In the current model, the same volume of air flows through the gap in a given time, even as that gap changes size; as the reed moves, the fluid velocity adjusts to maintain the flow rate.

We perform a linearization of the equation of motion for the reed, Eq. (5.7), to investigate the conditions under which the theory predicts small-amplitude oscillations. For small oscillations, the flow velocity always exceeds the reed velocity, so the

relative velocity is always in the downward direction, allowing us to take $\sigma = -1$. Setting $\dot{a} = \ddot{a} = 0$ gives an equation specifying the equilibrium state,

$$A(a^*)^2 a^* = -\frac{12C_1 F_1}{m_1^4 F_2} \frac{\rho L^4 Q^2}{Eh^3}$$

Combining this equation with (5.8) gives a formula for the equilibrium reed tip displacement in terms of the driving pressure,

$$a^* = -\frac{24C_1 F_1}{m_1^4 F_2} \frac{L^4 \Delta p}{Eh^3}.$$

We are interested in the behavior of small oscillations around this equilibrium. We linearize the second-order ODE at $a = a^*$, $\dot{a} = 0$,

$$M\ddot{a} + B\dot{a} + K(a - a^*) = 0,$$

where the coefficients M, B, and K are calculated to be

$$
\begin{aligned}
M &= \rho_r h + C_2 \rho W \\
B &= \frac{\rho Q}{A^*}\left(2C_1 - \frac{C_2 F_1 W A'^*}{F_2 A^*}\right) \\
K &= \frac{m_1^4 h^3 E}{12L^4} - \frac{2C_1 F_1 \rho Q^2 A'^*}{F_2 A^{*3}}.
\end{aligned}
$$

The area and its derivative at equilibrium, $A^* = A(a^*)$, $A'^* = A'(a^*)$, are calculated according to Eq. (5.3-5.4). The flow rate is given by Eq. (5.8).

Such a second-order system will undergo oscillations if the eigenvalues are complex, that is, if $B^2 < 4MK$, and their real part is positive, that is, $B < 0$. For our system, this second condition takes the form

$$W\frac{A'^*}{A^*} > \frac{2C_1 F_2}{C_2 F_1}. \tag{5.9}$$

To have oscillations, the quantity A'/A at the equilibrium point must exceed a certain constant. This quantity measures how much the gap area changes with reed tip

displacement. Physically, the force from the fluid acceleration must exceed the drag due to the motion of the reed itself. This occurs when the gap area changes sufficiently to accelerate the fluid.

This prediction is consistent with both major observations about free reeds. If a reed is mounted on the downstream side of the plate, the gap area decreases as the reed moves upstream. In this case $A'^* < 0$, so Eq. (5.9) can never be satisfied. Furthermore, for a reed on the upstream side of the plate, A'^*/A^* decreases as the equilibrium position moves farther from the plate. At some critical position, the ratio A'^*/A^* will fall below the required constant, precluding the possibility of oscillations. The frequency of oscillation can also be calculated from the coefficients,

$$\omega = \sqrt{\frac{K}{M} - \left(\frac{B}{2M}\right)^2}. \tag{5.10}$$

When this frequency is real, the eigenvalues are complex, which must be the case for oscillation to arise.

Fig. 5-1 illustrates a simulation of the second-order system, Eqs. (5.3), (5.7), and (5.8), at $\Delta p = 0.5\ kPa$. The behavior is qualitatively correct. However, the frequency is only 631.0 Hz, much lower than the measurements in Fig. 3-6. Fig. 5-2 shows a simulation at a higher pressure, $\Delta p = 1.0\ kPa$. In this simulation, the reed, after about 0.4 s, is pushed below the top of the support plate. This behavior seems to occur for all higher driving pressures as well. Since the magnitude of the fluid velocity is Q/A, it is not surprising that when the flow rate Q is fixed, the force on the reed is very large when the gap area A becomes small.

These results indicate that, under the assumption that the flow rate Q is constant, our model fails to adequately describe free reed oscillation. In the next section, we extend our model by allowing for a reed driven at a constant pressure to experience a time-varying flow rate $Q(t)$.
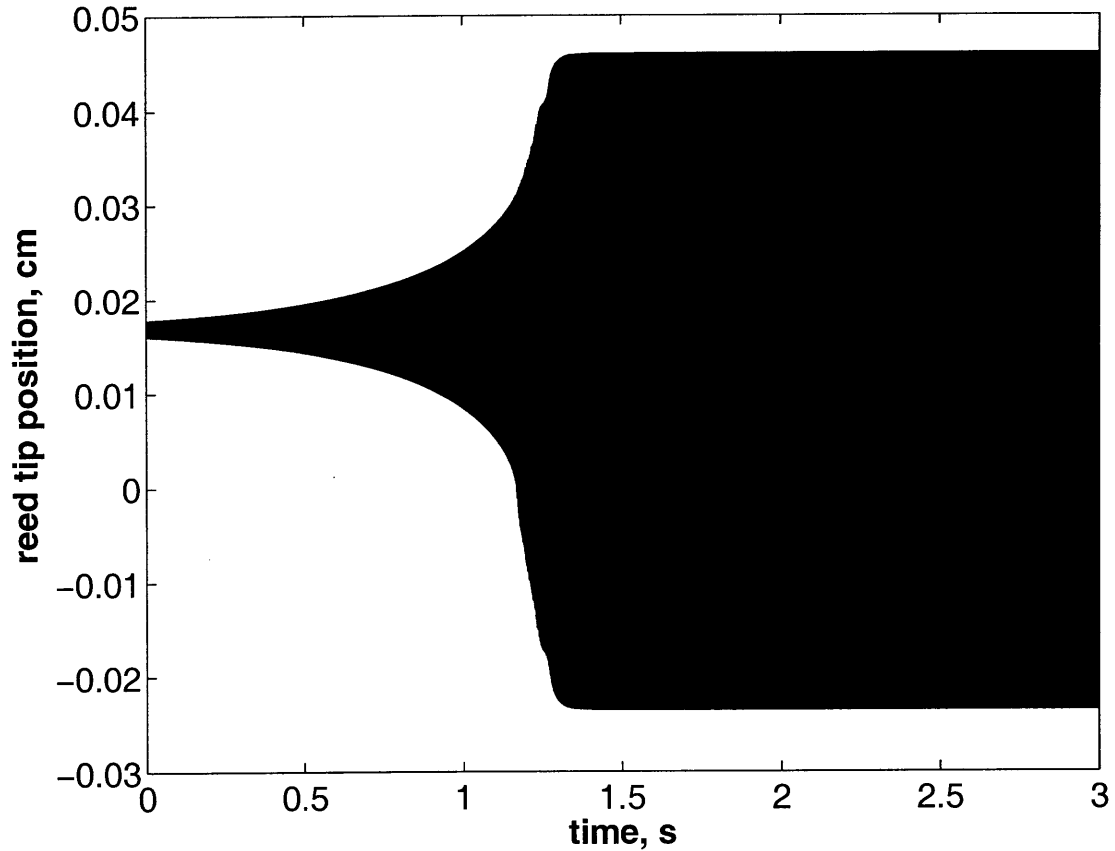
Figure 5-1: Simulation of a reed's oscillation, found by solving Eq. (5.3,5.7). The reed position $a_0 + a(t)$ is plotted. The reed parameters listed in Table 3.1 are used, with a driving pressure of 0.5 kPa determining the constant flow rate by Eq. (5.8). The best fit frequency, obtained from the simulation by fitting a line to the times corresponding to the reed position minima starting after the limiting amplitude has been reached, is 631.0 Hz.
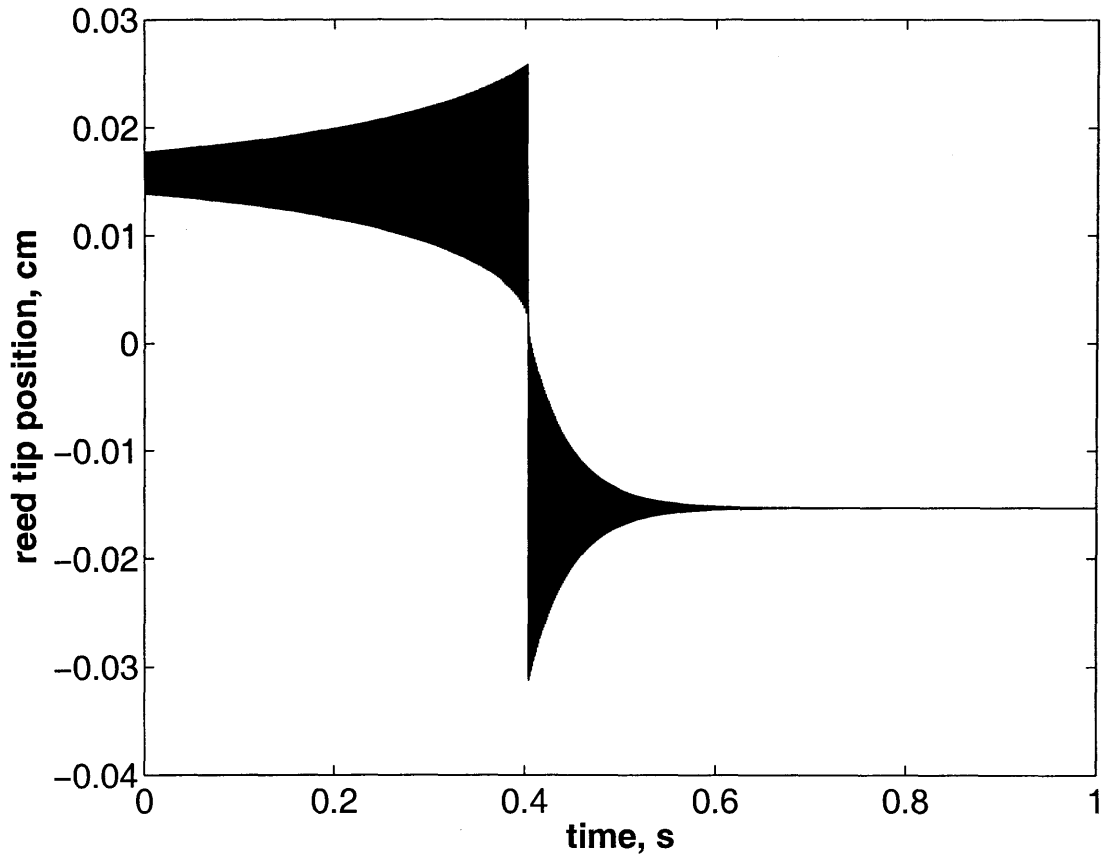
Figure 5-2: Simulation of the reed's oscillation, Eq. (5.3,5.7,5.8), driven at 1.0 kPa. At about 0.4 s, the reed is pushed below the top of the support plate, where it remains for the rest of the simulation, its amplitude decaying. The best fit frequency after it is pushed below the top of the plate is 751.6 Hz.

5.5 Time-varying flow rate

The deficiencies discussed so far suggest that we relax the assumption that the flow rate through the gap Q is constant and allow it to change in time, $Q(t)$. So far, our model includes the reed and the support plate but does not consider the source of the flow. In order to understand the dynamics of the flow rate, we must add a description of the reservoir that provides air to the reed. The nature of this reservoir is different for different instruments. In the case of an accordion or concertina, for example, the reed is driven by the air inside the bellows; for a harmonica, this reservoir would include the player's mouth and possibly also the player's throat and lungs. In our experimental setup, both the chamber to which the reed is mounted and the hose that feeds the chamber from the compressed air source must be considered.

A time-varying flow rate through the reed introduces the possibility of air accumulating in the chamber over the course of the reed's oscillation. We proceed by demonstrating that this effect is not significant. This would be significant if the corresponding changes in air density contribute to pressures of the same order as those predicted by the current theory. We argue that any such change in density has a negligible effect on the reed dynamics. We assume the worst, that the flow rate into the chamber is constant, making no attempt to adjust to the varying flow rate out of the chamber through the reed. We also assume the greatest possible variation in flow rate into the chamber, that is, that the flow rate drops to nearly zero when the reed goes into the support plate and increases in proportion to the reed's distance from the support plate. (This worst-case assumption would be the case if the flow rate had little inertia and therefore adjusted quickly to the reed's position.) Under these two assumptions, the magnitude of the net flow rate into or out of the chamber, ΔQ, is some order one multiple of the equilibrium flow rate Q_0. Using the steady Bernoulli formula to calculate Q_0 from the equilibrium gap area A_0,

$$Q_0 = A_0 \sqrt{\frac{2\Delta p}{\rho}}, \quad$$

we have that a net flow rate of up to

$$\Delta Q \sim A_0\sqrt{\Delta p/\rho}$$

may be entering or leaving the chamber. A volume of $\Delta Q/\omega$ may accumulate over the course of an oscillation, increasing the mass of the air in the chamber by $\rho\Delta Q/\omega$, and therefore the density by

$$\Delta\rho \sim \frac{\rho\Delta Q}{\omega V_c}.$$

We wish to know whether such density changes will affect the pressure in the chamber. Pressure differences are related to density differences by

$$\Delta P \approx \frac{dp}{d\rho}\Delta\rho.$$

Using $c^2 = dp/d\rho$, we find that the pressure can vary by an amount

$$\Delta P \sim \frac{c^2\rho A_0}{\omega V_c}\frac{\Delta p}{\rho}.$$

The ratio of this pressure perturbation to the driving pressure, which we take to be the magnitude of the dynamic pressures, is

$$\frac{\Delta P}{\Delta p} \sim \frac{c^2 A_0}{\omega V_c}\sqrt{\frac{\rho}{\Delta p}}.$$

For the 750 Hz reed in our setup, driven at 2 kPa, this ratio is

$$\frac{\Delta P}{\Delta p} \sim 9 \times 10^{-4}.$$

This indicates that we can safely neglect the pressure changes that would result from accumulation of air inside the chamber. This amounts to treating the air as incompressible for the purpose of calculating velocities and pressures.

Our apparatus is fed through a hose by a source of compressed air. We take the pressure at the source to be constant, p_s. The hose is connected to the base of the

chamber, where we assume the air enters as a jet, and therefore take the pressure at the jet equal to the pressure in the chamber near the entry point, p_c. The pressure drop along the length of the hose is therefore related to the flow rate $Q(t)$ by

$$p_s - p_c = R_h Q + \rho I_h \dot{Q}. \tag{5.11}$$

Here, we have incorporated terms for both the resistance (R_h) and inertia (I_h) of the air in the hose. For another model that incorporates these terms, see Bertram and Pedley's model of unsteady flow in collapsible tubes [8]. The air leaves the chamber as a jet through the gap between the reed and the support plate, whose pressure we therefore take to be atmospheric, p_0. This jet is moving much faster than the air in the chamber itself, whose velocity we therefore neglect. The pressure within the chamber is related to the flow rate by

$$p_c - p_0 = \frac{1}{2}\rho \left(\frac{Q}{A}\right)^2 + R_c Q + I_c \dot{Q}. \tag{5.12}$$

R_c and I_c are the coefficients for the resistance and inertia of the air in the chamber. Adding Eq. (5.11) and Eq. (5.12) gives an ODE for $Q(t)$,

$$(I_h + I_c)\dot{Q} + (R_h + R_c)Q + \frac{1}{2}\rho \left(\frac{Q}{A}\right)^2 = p_s - p_0. \tag{5.13}$$

The resistance $R_h = \Delta P / Q$ of the hose can be estimated from its radius $r_h \approx 0.5\ cm$ and length $L_h \approx 4\ m$ using Poiseuille's law[33],

$$R_h = \frac{8\mu L_h}{\pi r_h^4} \approx 3\ g cm^{-4} s^{-1}. \tag{5.14}$$

The inertia of the air in the hose can be calculated by applying the time-dependent Bernoulli equation to each end of the hose:

$$p_s + \rho \frac{d\phi_s}{dt} = p_c + \rho \frac{d\phi_c}{dt}$$

Here, ϕ_s is the value of the velocity potential at the source end of the hose and ϕ_c

is its value at the chamber end. Assuming uniform flow throughout the hose, the velocity potential as a function of distance x from the source end is

$$\phi(x) = \frac{Q}{\pi r_h^2} x.$$

Their difference is therefore $\phi_c - \phi_s = QL_h/\pi r_h^2$, giving a formula for the inertia coefficient $I_h = \Delta P/\dot{Q}$,

$$I_h = \frac{\rho L_h}{\pi r_h^2} \approx 0.6 \ gcm^{-4}. \tag{5.15}$$

We can make a similar estimate for the resistance of the chamber, but since the chamber's dimensions are so much larger, it's clear from the form of R_h that the hose's resistance will dominate the chamber's. We can also make an estimate for the inertia of the air in the chamber, although this is more difficult because the flow ceases to be uniform as it approaches the reed. The inertia of the uniform region will clearly be dominated by that of the hose, so can be safely neglected. We can make a crude estimate for the flow entering the reed gap by taking it to be a line sink with out-of-plane length L corresponding to the length of the reed. The velocity potential of this line sink would be, as a function of radial distance from the reed r,

$$\phi(r) = -\frac{Q}{\pi L} \log r.$$

It is unclear exactly where the flow transitions from this form to the constant-pressure jet, but an estimate would have the line sink extend from the equilibrium reed position $r = a_0$ to one reed length away, $r = L$. For our reed with $a_0 \approx 0.02 \ cm$ and $L \approx 2 \ cm$, the inertia coefficient $\Delta P/\dot{Q}$ for this region would then be

$$\frac{\rho}{\pi L} \log \frac{L}{a_0} \approx 0.0007 \ gcm^{-4},$$

indicating that the inertia of this flow is also dominated by that of the air in the hose, regardless of whether this estimate captures the precise form of the flow. We therefore neglect both the resistance and inertia of the air in the chamber. This approximation

also implies that the pressure we measure in the chamber is approximately equal to the source pressure. We therefore take the driving pressure measured by our pressure gauge to be $\Delta p = p_s - p_0$.

To simplify Eq. (5.13) even further, we calculate the ratio of the resistance term to the inertia term. Substituting in the values of R_h and I_h, and using the reciprocal of our reed frequency, 750 Hz, for a time scale, we obtain $RQ/I\dot{Q} \sim 0.008$. We therefore neglect the resistance term, resulting in a simple ODE for the flow rate $Q(t)$,

$$I\dot{Q} + \frac{1}{2}\rho \left(\frac{Q}{A}\right)^2 = \Delta p, \qquad (5.16)$$

where I is the value I_h from Eq. (5.15). It should be noted that there is a large degree of uncertainty in the value of I, because the relationship between pressure and flow rate at the source is not clear. Also, the value of I will be different for different experimental setups, depending as it does on the detailed geometry of the reservoir.

5.6   Comparison with experiment

We supplement the second-order system for the reed's position $a(t)$, Eqs. (5.3) and (5.7), with the first-order equation for the flow rate $Q(t)$, Eq. (5.16), giving a third-order model. In this section, we consider whether this model can describe the oscillations of free reeds.

Fig. 5-3 shows a simulation of the third-order model, Eq. (5.3,5.7,5.16), using $\Delta p = 1 \; kPa$ for the driving pressure and $I = 0.6 \; gcm^{-1}$ for the inertia coefficient in Eq. (5.16). There is apparently a short period at the beginning of the simulation during which the flow rate, whose initial value is set by the unforced gap area, adjusts to a lower value. In contrast to the simulation in Fig. 5-2, the reed is not pushed below the top of the support plate. Furthermore, the simulated frequency, 744.2 Hz, is within the range measured in the experiments described in Fig. 3-6.

Fig. 5-4 shows the waveforms of the reed position and flow rate. The position waveform is sinusoidal, consistent with the results of Cottingham [15]. The form of
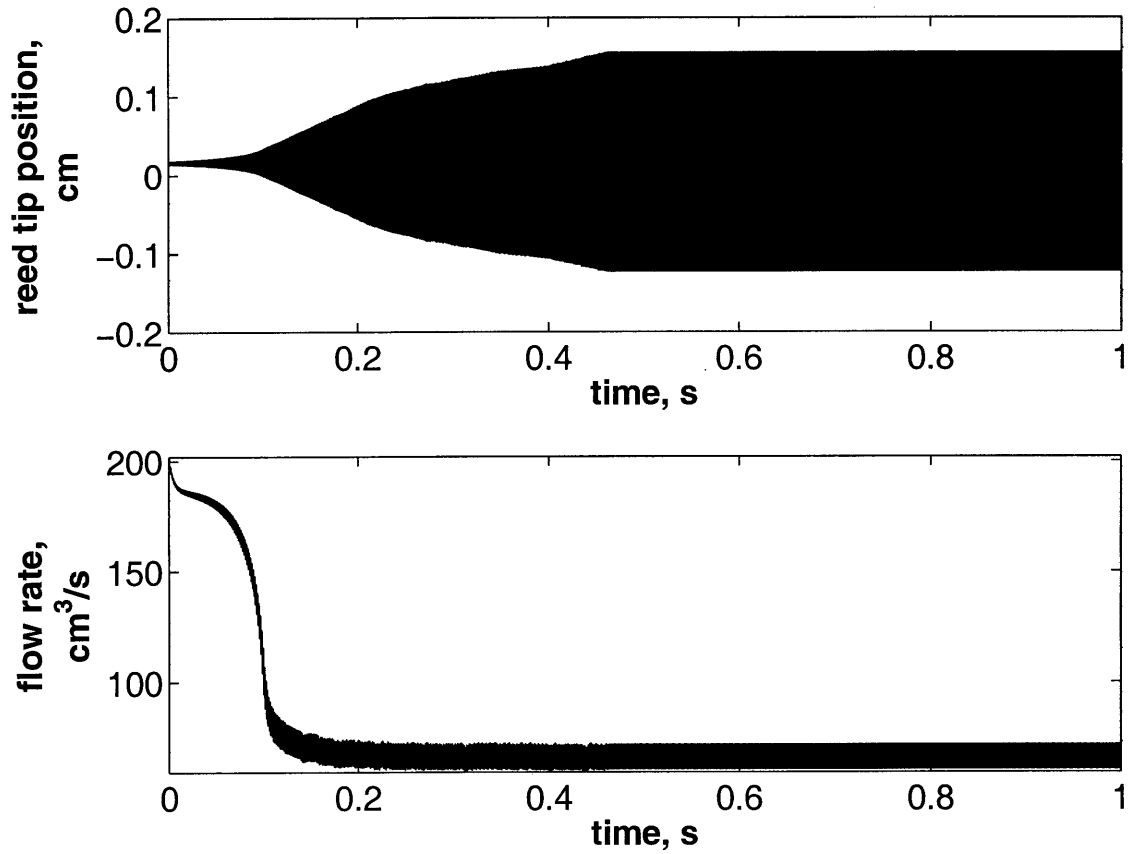
76

Figure 5-3: Simulation of the reed's oscillation using the third-order model, Eq. (5.3,5.7,5.16), using $I = 0.6 \ gcm^{-1}$ for the inertia coefficient. The reed's position $a_0 + a(t)$ is plotted above, the flow rate $Q(t)$ below. The reed was driven at $\Delta p = 1 \ kPa$. The best fit frequency is 744.2 Hz.
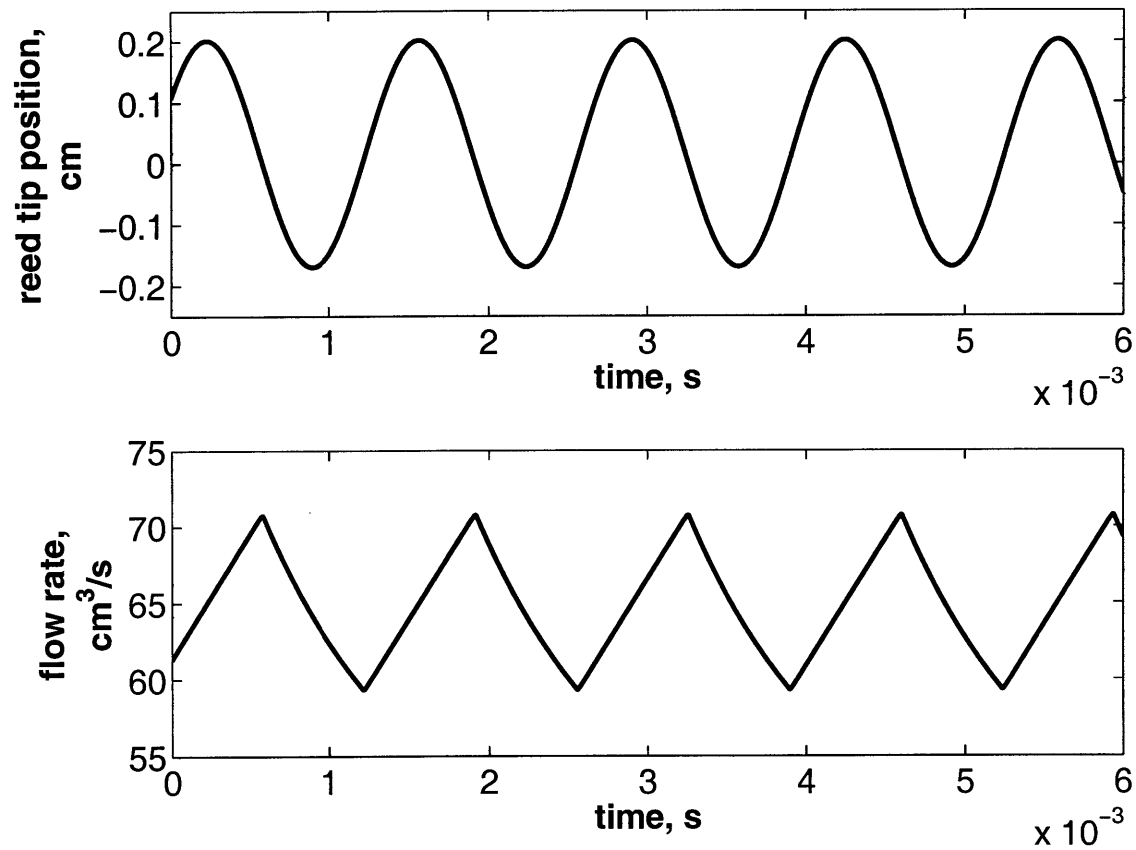
Figure 5-4: Simulated waveforms of reed position (top) and flow rate (bottom) over several oscillations, using the third-order model, for the same conditions as Fig. 5-3. Note that the reed position and flow rate are both periodic, but that the flow rate lags a fraction of a period behind the reed position.
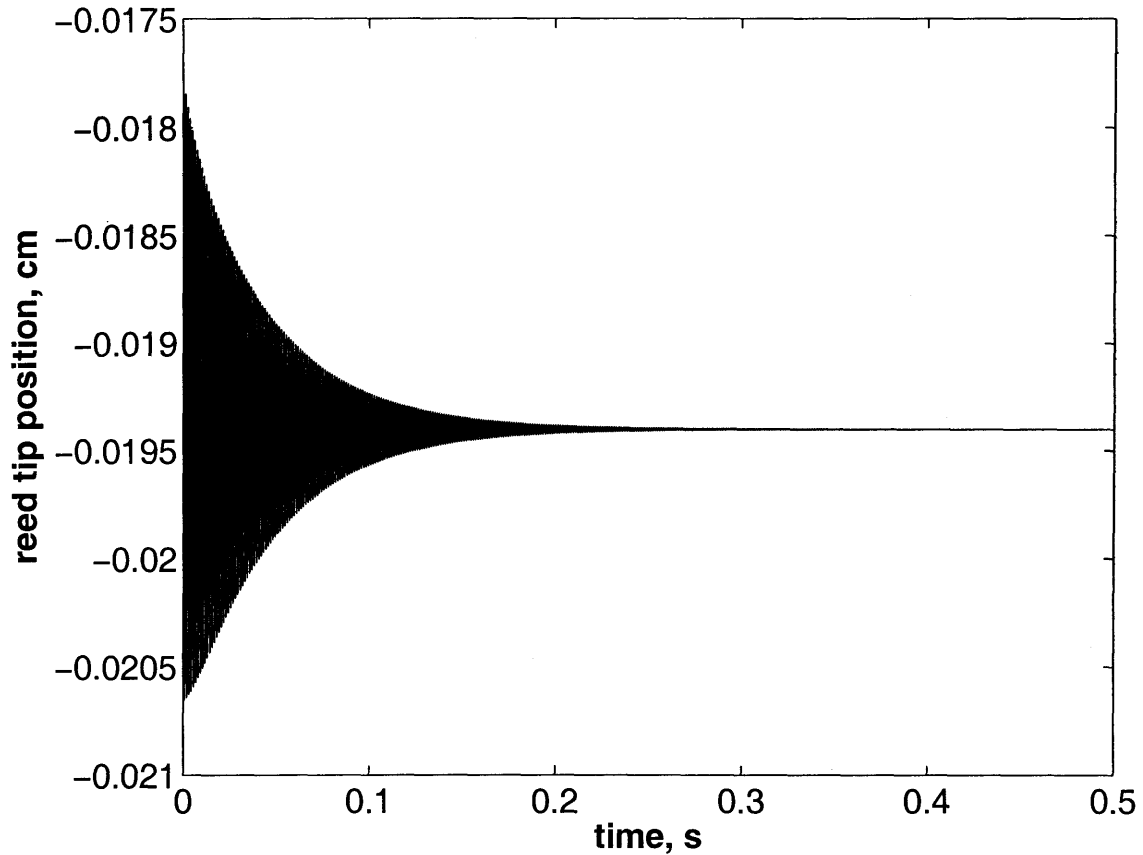
Figure 5-5: A reed driven by airflow in the wrong direction, simulated using the third-order model. The same parameters from Table 3.1 are used, except the equilibrium position a_0 is taken to be $-0.02\ cm$; that is, the reed is initially below the bottom of the support plate. Eq. (5.3) is corrected so that the gap area drops to its minimum when the reed position $a_0 + a$ exceeds zero. The reed is driven at $1\ kPa$ using $I = 0.6\ gcm^{-4}$. The frequency of oscillation is $800.2\ Hz$.

the flow rate looks different from that measured in Cottingham's experiments, but it does bear some similarity to our own (Fig. 3-5). Comparison of the reed position and flow rate plots reveals an interesting fact: The flow rate appears to lag behind the reed position by a sizable fraction of a period. This is understandable now that we are taking into account the inertia of the air in the reservoir; the flow rate takes time to adjust to the current size of the gap. Therefore, when the reed is moving away from the support plate, the flow rate is lower than when it is moving towards the support plate. The result is an asymmetrical distribution of force on the reed, greater when the reed is moving towards the plate and smaller when it is moving away. For a reed positioned on the upstream side of its support plate, the unsteady component of the force is in the direction of the reed's motion, driving its oscillations. For a reed positioned on the downstream side, the unsteady component of the force is opposed to the reed's motion, damping its oscillations. In Fig. 5-5, we verify that the theory predicts this behavior for a reed on the downstream side of its support plate, a further check that this model gives behavior consistent with real free reeds.

In Fig. 5-6, we plot the dependence of amplitude and frequency on driving pressure. Because the value of the I parameter would differ between setups, and is uncertain even for our setup, we performed simulations at different values of I. Several discrepancies are evident. First, the slope of the frequency versus pressure plot does not match the measured slopes shown in Fig. 3-6. Second, for one of the values of the inertia coefficient, $I = 0.1 \ gcm^{-4}$, the amplitude quickly grows to over 1 cm, much higher than the observed amplitude, which is at most several millimeters. This value of I would be expected in a setup with a shorter hose, for example. Further work is required to understand these discrepancies. Perhaps the amplitude is kept small by damping not considered in our model.

We have introduced two models of free reeds that predict oscillations: The second-order model described by Eq. (5.3,5.7,5.8) relies on a force due to the fluid's acceleration, while the third-order model described by Eq. (5.3,5.7,5.16) also incorporates a time-varying flow rate. The second-order model predicts oscillation frequencies much lower than those observed and breaks down when the reed's amplitude allows it to pass
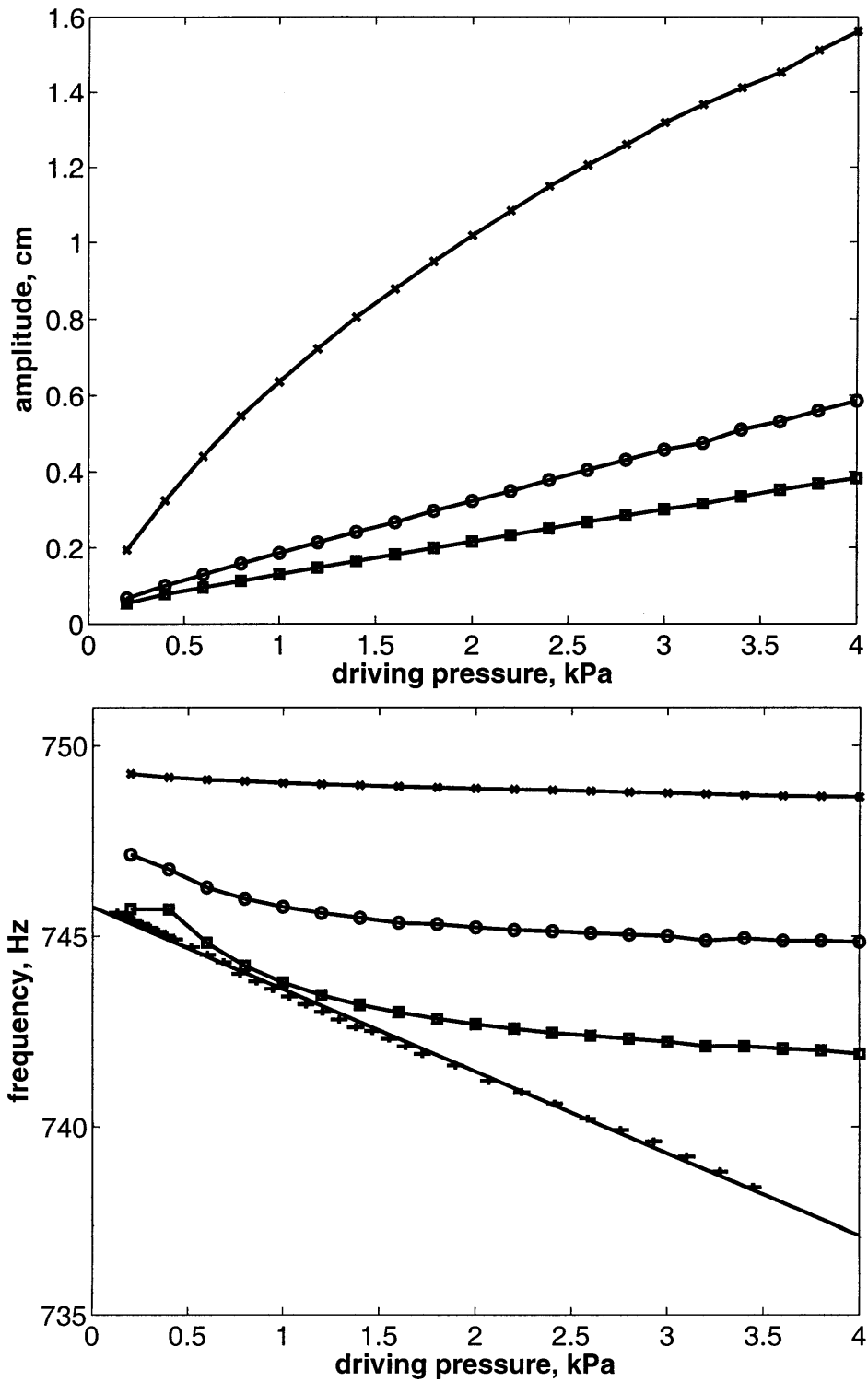
Figure 5-6: Dependence of simulated amplitude and frequency on driving pressure, using the reed parameters from Table 3.1, for various values of the inertia coefficient, $I = 0.1\ gcm^{-4}$ (x), $I = 0.6\ gcm^{-4}$ (o), and $I = 1.0\ gcm^{-4}$ (□). Amplitude shown is half the difference between the maximum and minimum simulated reed position. The amplitudes and frequencies for the lowest pressures may be slightly off due to the slow growth at these pressures. Frequency measurements from the first data set in Fig. 3-6 are also shown (+).

under the top of the support plate (Fig. 5-2). The third-order model does not break down for large driving pressures and predicts more realistic frequencies, although it involves the parameter I, whose value is uncertain and depends on the geometry of the air reservoir. Further study, and more exact comparison to experiments, is definitely required.

Chapter 6

Conclusion

We have considered two physical systems with several common features: structures that can be described by the theory of elastic beams and unsteady flows in which wakes are present. In both systems, steady imposed flows produce oscillations of the structure, and the goal was to elucidate the mechanism responsible for the oscillations and construct theoretical models that describe experiment. The challenges in the two problems turned out to be different: In the clapping book, the large-amplitude deformations of the structure necessitated nonlinear equations, and the presence of multiple sheets required determining how the sheets interact. For free reeds, the principal difficulty was modeling and measuring high-speed flow over small structures with complicated geometry.

For the clapping book, we have successfully described the shapes of elastic sheets in flow using the theory of finite-amplitude deformations of slender beams, which we applied to both individual elastic sheets and stacks of paper. Our model predicts the critical wind speed below which a sheet falls, which we used to fit the drag coefficient and calculate the number of pages required for the clapping book to begin to collapse. We combined this with a heuristic description of page liftoff and simulations of page collapse in order to obtain a complete picture of the clapping process. We tested our predicted clapping period and found good agreement.

Our study of free reeds was motivated by a desire to explain two qualitative features of reed oscillation, that Western free reeds only oscillate when on the upstream

side of the support plate, and that they must be near the support plate to oscillate. We also sought a model that predicted realistic amplitudes, matched the frequencies we measured, and produced waveforms that resembled the ones we recorded. Our work was directed by several previous workers' observations: The amplitude growth is exponential [30], suggesting a quasistatic model of the flow; the reed oscillates primarily in its first mode [16], simplifying our analysis; and a wake is present downstream of the reed [30], which lead us to eventually abandon the potential flow model.

Our first attempt (Chapter 4), motivated by recent work in conformal mapping on multiply connected domains, failed in describing the problem using potential flow, but identified the acceleration of the fluid as potentially important to the mechanism. This prompted a second attempt, introduced in Sections 5.1-5.4, which used a more realistic, if less exact, description of the flow, which took into account the presence of a wake. It successfully explained the qualitative features of reed oscillation but failed to produce quantitative agreement with measurements. Our third theory, introduced in Section 5.5, included a description of the flow of air within the reservoir, and required the introduction of an additional parameter. This theory seems likely to give quantitative agreement with measurements, although more experimental work is still required.

In retrospect, a better way to approach the free reeds problem would have been to first make measurements and then use data to construct a theory, rather than to make a guess at a theory and try to modify it to get the data to fit. Both the potential flow model (Chapter 4) and the second-order ODE model (Sections 5.1-5.4) were interesting to develop but did not end up relating to real free reeds; both omit ingredients (the wake behind the reed and a time-varying flow rate) that we now think are necessary to describe the problem.

Given the ubiquity of the interaction of flexible bodies and high Reynolds number flow in nature, we hope that the approaches developed for these problems will find wider application in the biological sciences.

Bibliography

[1] D. J. Acheson. *Elementary Fluid Dynamics*, chapter 4. Oxford, 1990.

[2] S. Alben. Simulating the dynamics of flexible bodies and vortex sheets. *J. Comput. Phys.*, 228:2587–2603, 2009.

[3] S. Alben, M. Shelley, and J. Zhang. Drag reduction through self-similar bending of a flexible body. *Nature*, 420, December 2002.

[4] S. Alben, M. Shelley, and J. Zhang. How flexibility induces streamlining in a two-dimensional flow. *Phys. Fluids*, 16(5), May 2004.

[5] S. Alben and M. J. Shelley. *Phys. Rev. Lett.*, 100(074301), 2008.

[6] M. Argentina and L. Mahadevan. Fluid-flow-induced flutter of a flag. *Proceedings of the National Academy of Sciences of the USA*, 102(6):1829–1834, February 2005.

[7] J. Backus. Small-vibration theory of the clarinet. *J. Acoustical Soc. of America*, 35(3), March 1963.

[8] C. D. Bertram and T. J. Pedley. A mathematical model of unsteady collapsible tube behaviour. *J. Biomech.*, 15:39–50, 1982.

[9] P. Buchak and J. Bush. Flow-induced oscillation of free reeds. *(in preparation)*, 2010.

[10] P. Buchak, C. Eloy, and P. Reis. The clapping book: wind-driven oscillations in a stack of elastic sheets. *Phys. Rev. Lett (submitted for publication)*, 2010.

[11] C. Cancelli and T. Pedley. A separated-flow model for collapsible-tube oscillations. *J. Fluid Mech.*, 1985. See equations (18).

[12] S. Childress. *Mechanics of swimming and flying*. Cambridge, 1981.

[13] B. Coleman, E. Dill, M. Lembo, Z. Lu, and I. Tobias. *Arch. Rational Mech. Anal.*, 121:339–359, 1993.

[14] J. P. Cottingham. Pitch bending and anomalous behavior in a free reed coupled to a pipe resonator. In *Proceedings of the International Symposium on Musical Acoustics (ISMA2007), Barcelona, Spain*, September 2007.

[15] J. P. Cottingham. Reed vibration in western free-reed instruments. In *Proceedings of the International Congress on Acoustics, Madrid, Spain*, September 2007.

[16] J. P. Cottingham, C. J. Lilly, and C. H. Reed. The motion of air-driven free reeds. In *Collected Papers of the 137th meeting of The Acoustical Society of America and the 2nd Convention of the European Acoustics Association: Forum Acusticum, Berlin*, March 1999.

[17] J. P. Cottingham, C. H. Reed, and M. Busha. Variation of frequency with blowing pressure for an air-driven free reed. In *Collected Papers of the 137th meeting of The Acoustical Society of America and the 2nd Convention of the European Acoustics Association: Forum Acusticum, Berlin*, March 1999.

[18] D. Crowdy. (private communication).

[19] D. Crowdy and P. Buchak. (in preparation).

[20] D. G. Crowdy. *European Journal of Mechanics B*, 25:459–470, 2006.

[21] D. G. Crowdy. Schwarz-christoffel mappings to unbounded multiply connected polygonal regions. *Math. Proc. Camb. Phil. Soc.*, pages 319–339, 2007.

[22] D. G. Crowdy, A. Surana, and K-Y. Yick. *Phys. Fluids*, 19(018103), 2007.

[23] E. de Langre. Effect of wind on plants. *Annu. Rev. Fluid Mech.*, 40:141–68, 2008.

[24] K. Drescher, K. Leptos, I. Tuval, T. Ishikawa, T. Pedley, and R. Goldstein. Dancing volvox: Hydrodynamic bound states of swimming algae. *Phys. Rev. Lett.*, 102(168101), 2009.

[25] N. H. Fletcher. Excitation mechanisms in woodwind and brass instruments. *Acustica*, 43, 1979.

[26] N. H. Fletcher and T. D. Rossing. *The physics of musical instruments*. Springer, 1991.

[27] M. Ghisalberti and H. Nepf. Shallow flows over a permeable medium: the hydrodynamics of submerged aquatic canopies. *Transport in Porous Media*, 78(385-402), 2009.

[28] Greenspan and Benney. *Calculus: An Introduction to Appl. Math.*, page 555. 1997.

[29] H. L. F. Helmholtz. *On the sensations of tone*. 1877.

[30] Arthur O. St Hilaire, Theodore A. Wilson, and Gordon S. Beavers. Aerodynamic excitation of the harmonium reed. *J. Fluid Mech.*, 49(4):803–816, 1971.

[31] R. B. Johnston. Pitch control in harmonica playing. *Acoustics Australia*, 15:69–75, 1987.

[32] Katz, Chen, and Moreno. Flow through a collapsible tube. *Biophysics J.*, 1969.

[33] Pijush K. Kundu and Ira M. Cohen. *Fluid Mechanics, Third Edition*, page 285. Elsevier, 2004.

[34] L. D. Landau and E. M. Lifshitz. *Theory of Elasticity.* 1959.

[35] M. J. Lighthill. *J. Fluid Mech.*, 9(2), 1960.

[36] D. Lisoski. *Nominally two-dimensional flow about a normal flat plate.* PhD thesis, California Institute of Technology, 1993.

[37] A. Manela and M. S. Howe. On the stability and sound of an unforced flag. *J. of Sound and Vibration*, 2008.

[38] L. M. Milne-Thomson. *Theoretical Hydrodynamics*, chapter 12. Macmillan, 1960.

[39] T. Pedley. *The fluid mechanics of large blood vessels.* 1980.

[40] T. J. Pedley and J. O. Kessler. Hydrodynamic phenomena in suspensions of swimming microorganisms. *Annu. Rev. Fluid Mech.*, 24:313–58, 1992.

[41] T. J. Pedley and X. Y. Luo. Modelling flow and oscillations in collapsible tubes. *Theoretical and Computational Fluid Dynamics*, 10:277–294, 1998.

[42] E. M. Purcell. Life at low reynolds number. *Am. J. Phys.*, 45(1), 1977.

[43] C. Py, E. de Langre, and B. Moulia. A frequency lock-in mechanism in the interaction between wind and crop canopies. *J. Fluid Mech.*, 568:425–449, 2006.

[44] J. W. S. Rayleigh. *The Theory of Sound*, volume 1. 1878.

[45] L. Schouveiler and C. Eloy. Coupled flutter of parallel plates. *Phys. Fluids*, 21(081703), 2009.

[46] L. Schouveiler, C. Eloy, and P. Le Gal. *Phys. Fluids*, 17(047104), 2005.

[47] M. Sherry, D. Jacono, J. Sheridan, R. Mathis, and I. Marusic. In *Sixth International Symposium on Turbulence and Shear Flow Phenomena*, 2009.

[48] D. Tam, J. W. M. Bush, M. Robitaille, and A. Kudrolli. Tumbling dynamics of passive flexible wings. *Phys. Rev. Lett.*, 104(184504), 2010.

[49] G. Taylor. Analysis of the swimming of long and narrow animals. *Proc. Roy. Soc. A*, pages 158–183, 1952.

[50] S. Vogel. *Life in Moving Fluids.* Princeton, 1994.

[51] Z. Jane Wang. Dissecting insect flight. *Annu. Rev. Fluid Mech.*, 37:183–210, 2005.

[52] D. Wilhelm and L. Kleiser. *J. Scientific Computing*, 17:1–4, 2002.